

A Hybrid Neural Network-Finite Element Method for the Viscous-Plastic Sea-Ice Model

Nils Margenberg* Carolin Mehlmann*

December 11, 2025

We present an efficient hybrid Neural Network–Finite Element Method (NN-FEM) for solving the viscous–plastic (VP) sea-ice model. The VP model is widely used in climate simulations to represent large-scale sea-ice dynamics. However, the strong nonlinearity introduced by the material law makes VP solvers computationally expensive, with the cost per degree of freedom increasing rapidly under mesh refinement. High spatial resolution is particularly required to capture narrow deformation bands known as linear kinematic features in viscous-plastic models. To improve computational efficiency in simulating such fine-scale deformation features, we propose to enrich coarse-mesh finite element approximations with fine-scale corrections predicted by neural networks trained with high-resolution simulations. The neural network operates locally on small patches of grid elements, which is efficient due to its relatively small size and parallel applicability across grid patches. An advantage of this local approach is that it generalizes well to different right-hand sides and computational domains, since the network operates on small subregions rather than learning details tied to a specific choice of boundary conditions, forcing, or geometry. The numerical examples quantify the runtime and evaluate the error for this hybrid approach with respect to the simulation of sea-ice deformations. Applying the learned network correction enables coarser-grid simulations to achieve qualitatively similar accuracy at approximately 11 times lower computational cost relative to the high-resolution reference simulations. Moreover, the learned correction accelerates the Newton solver by up to 10 % compared to runs without the correction at the same mesh resolution.

1. Introduction

The sea-ice cover in both hemispheres is characterized by narrow, elongated deformation zones known as linear kinematic features (LKF) [17]. These structures, which correspond to leads and pressure ridges, are important for the heat exchange between ocean, and atmosphere [24]. Accurately capturing LKFs in sea-ice models critically depends on the choice of sea-ice rheology [13]. Currently, most climate models apply the viscous–plastic (VP) constitutive relation [2], although several alternative rheological formulations have been proposed, e.g. [30]. Recent studies have shown that VP-based models can reproduce key statistical and scaling properties of observed LKFs [12].

*University of Magdeburg, Institute for Analysis and Numerics, Universitätsplatz 2, 39104 Magdeburg, Germany,
 {nils.margenberg, carolin.mehlmann}@ovgu.de

The nonlinearity introduced by the viscous–plastic material law makes solving the equations computationally expensive, with the computational cost per degree of freedom increasing rapidly as the mesh is refined [15, 31]. At high horizontal mesh resolution the computational cost of converged numerical sea-ice approximations can become as expensive as running the global ocean model [15]. Since mesh resolution is a key factor determining both the accuracy and computational cost of simulating linear kinematic features (LKF), we investigate whether a neural network can help to achieve qualitatively similar LKF patterns within the viscous–plastic sea-ice model on coarser horizontal grids, thereby reducing the overall computational cost of sea-ice–ocean simulations run at high spatial mesh resolution.

In addition to grid resolution, the simulation of LKFs in the viscous–plastic model depends on several factors, including solver convergence [15, 18], rheological parameters [12], wind forcing [11], and numerical spatial discretization [26]. Most sea-ice models use structured quadrilateral meshes, such as the *Community Ice Code* (CICE) [10], where velocities and stresses are discretized with bilinear finite element basis functions, or the *Massachusetts Institute of Technology general circulation model* (MITgcm) [19], which employs a finite-volume scheme with central differences. Recent developments introduce unstructured triangular finite element meshes, as in the *Finite-Volume Sea-Ice–Ocean Model* (FESOM) [3] and the sea-ice module of the *Icosahedral Nonhydrostatic Weather and Climate Model* [25], or quasi-structured finite-volume approaches, as used in the *Finite-Volume Community Ocean Model* (FVCOM) and the *Model for Prediction Across Scales* (MPAS) [8, 29].

Approach and Related Work We formulate the method within a finite element discretization framework. The proposed hybrid neural network–finite element approach enriches robust, converged coarse-mesh solutions with fine-scale corrections predicted by a neural network trained on high horizontal resolution data. The core idea is to project the coarse-scale solution onto a refined mesh obtained through grid refinement. On this fine mesh, the neural network refines the solution and generates an updated right-hand side for the sea-ice momentum equation. This updated field is then projected back onto the coarse mesh and used to advance the simulation in the next time step. Owing to the locality of the finite element discretization (i.e., its compact stencil), the neural network operates locally, making the method particularly well suited for learning spatially localized structures such as linear kinematic features (LKF). Furthermore, the localized nature of the approach renders it attractive for large-scale parallel computing architectures used in climate simulations. The concept is closely related to hybrid finite element–neural network methods developed to enhance coarse-scale approximations of the Navier–Stokes equations [22, 23]. A dynamic super-resolution approach was recently proposed for the shallow-water equations, in which a U-Net is used to correct coarse ICON-O simulations [33]. This method achieves errors comparable to those of a mesh twice as fine while preserving key flow balances. This concept is closely aligned with our hybrid correction philosophy. Machine learning has recently been applied to sea-ice modeling to improve subgrid-scale representation and forecasting. Finn *et al.* used U-Net-based corrections for a Maxwell elasto-brittle sea-ice rheology, reducing forecast errors by over 75% [7]. Durand *et al.* developed CNN surrogates for long-term sea-ice thickness prediction, outperforming persistence and climatology baselines [5].

Contributions and Limitations Our contributions are threefold. First, we explore the concept of the multiscale hybrid finite element–neural network in the context of the highly nonlinear viscous–plastic sea-ice model and evaluate its performance with respect to the simulation of LKFs and the computational cost. The results show that our method achieves high accuracy while reducing time-to-solution relative to high resolution reference simulations. Second, we perform detailed ablation studies that investigate the importance of the network’s input quantities. Third, we generalize the use of neural networks beyond mesh cells, allowing them to operate locally on small patches of mesh elements. We

provide computational studies on the impact of patch size and number of predicted levels.

The presented hybrid neural network-finite element method (NN-FEM) strongly depends on the hierarchical mesh structure and the locality of the finite element approach to relate the coarse-scale approximation with the fine-scale counterpart. Nevertheless, it is flexible regarding the numerical discretization details: the coarse-grid problem can be solved with various standard solvers, and the local enrichment via neural networks could be done without constructing a global fine grid. Other local discretization methods such as finite differences or finite volumes might also be a suitable setup. The NN-FEM is presented on quadrilateral mesh in the context of the viscous-plastic rheology. We are confident that the method can be applied to nested triangular meshes and be used with different sea-ice rheologies.

2. Governing Equations

Let $\Omega \subset \mathbb{R}^2$ be a bounded Lipschitz domain and $I = (0, T] \subset \mathbb{R}$ be the time interval of interest. The sea-ice dynamics in the classical viscous-plastic sea-ice model of Hibler [9] is prescribed by three variables: the horizontal velocity $\mathbf{v} : \Omega \times I \rightarrow \mathbb{R}^2$, the thickness $H : \Omega \times I \rightarrow [0, \infty)$ and the concentration $A : \Omega \times I \rightarrow [0, 1]$. The equations of motion are given by the following system.

$$\rho_{\text{ice}} H \left(\partial_t \mathbf{v} + f_c \mathbf{e}_z \times (\mathbf{v} - \mathbf{v}_w) \right) = \text{div} \boldsymbol{\sigma} + \boldsymbol{\tau}(\mathbf{v}), \quad (1a)$$

$$\partial_t A + \text{div}(\mathbf{v} A) = 0, \text{ in } \Omega \times I, \quad (1b)$$

$$\partial_t H + \text{div}(H \mathbf{v}) = 0, \text{ in } \Omega \times I, \quad (1c)$$

where ρ_{ice} is the sea-ice density, f_c the Coriolis parameter, \mathbf{e}_z the out-of-plane unit vector ($\mathbf{e}_z \times (v_1, v_2) = (-v_2, v_1)$) and \mathbf{v}_w the near surface ocean velocity. The stress $\boldsymbol{\sigma}$ is given by the VP rheology (4). We use div for the divergence on vectors and the row-wise divergence on second-order tensors; spatial derivatives are with respect to $x \in \Omega$. We neglect the thermodynamics. Therefore, there are no source and sink terms in the balance laws (1b) and (1c).

Drag Forces. The oceanic and atmospheric drag forces $\boldsymbol{\tau}(\mathbf{v})$ (force per unit horizontal area) are given by

$$\boldsymbol{\tau}(\mathbf{v}) = \boldsymbol{\tau}_w(\mathbf{v}) + \boldsymbol{\tau}_a(\mathbf{v}), \quad (2)$$

with $\boldsymbol{\tau}_w(\mathbf{v}) = C_w \rho_w \|\mathbf{v}_w - \mathbf{v}\|_2 (\mathbf{v}_w - \mathbf{v})$ and $\boldsymbol{\tau}_a = C_a \rho_a \|\mathbf{v}_a\|_2 \mathbf{v}_a$. Here, $\rho_w, \rho_a > 0$ are water and air densities, $C_w, C_a > 0$ dimensionless drag coefficients, and $\mathbf{v}_w, \mathbf{v}_a : \Omega \times I \rightarrow \mathbb{R}^2$ prescribed the near surface atmospheric and oceanic flows.

VP Rheology. The viscous-plastic rheology relates internal stresses $\boldsymbol{\sigma}$ to strain rates

$$\dot{\boldsymbol{\epsilon}} := \frac{1}{2} (\nabla \mathbf{v} + \nabla \mathbf{v}^\top) \quad \dot{\boldsymbol{\epsilon}}' := \dot{\boldsymbol{\epsilon}} - \frac{1}{2} \text{tr}(\dot{\boldsymbol{\epsilon}}) I, \quad (3)$$

where tr denotes the trace, $\dot{\boldsymbol{\epsilon}}'$ is the deviatoric part and I the identity matrix. The viscous-plastic constitutive relation reads as follows.

$$\boldsymbol{\sigma} = 2\eta \dot{\boldsymbol{\epsilon}}' + \zeta \text{tr}(\dot{\boldsymbol{\epsilon}}) I - \frac{P}{2} I. \quad (4)$$

The viscosities, η, ζ , and sea-ice strength, P , are given as

$$\eta = e^{-2} \zeta, \quad \zeta = \frac{P}{2\Delta(\boldsymbol{\epsilon})}, \quad P(H, A) = P^* H \exp(-C(1 - A)). \quad (5)$$

Here, $e = 2$ denotes the eccentricity of the elliptical yield curve and P^*, C are the ice strength parameters. To achieve a smooth transition between the viscous and the plastic regime, we follow [16, 27] and choose the following regularization:

$$\Delta(\dot{\epsilon}) = \sqrt{\Delta_P(\dot{\epsilon})^2 + \Delta_{\min}^2}. \quad (6)$$

In case of the plastic regime, $\Delta_P(\dot{\epsilon})$ is defined as

$$\Delta_P(\dot{\epsilon}) = \sqrt{\frac{2}{e^2} \dot{\epsilon}' : \dot{\epsilon}' + (\text{tr}(\dot{\epsilon}))^2}, \quad (7)$$

whereas the viscous regime is given as

$$\Delta_{\min}(\dot{\epsilon}) = 2 \times 10^{-9}. \quad (8)$$

Initial and Boundary Data. The system is completed by prescribing the following initial and boundary data.

$$\begin{aligned} \mathbf{v} &= \mathbf{v}_0 && \text{on } \{t = 0\} \times \Omega, \\ A &= A_0, \quad H = H_0 && \text{on } \{t = 0\} \times \Omega, \\ \mathbf{v} &= 0 && \text{on } I \times \partial\Omega, \\ A &= A^{\text{in}}, \quad H = H^{\text{in}} && \text{on } I \times \Gamma^{\text{in}}, \end{aligned}$$

where $\Gamma^{\text{in}} := \{x \in \partial\Omega \mid \mathbf{n} \cdot \mathbf{v} < 0\}$ and \mathbf{n} is the outward unit vector.

Variational Formulation. In order to apply a finite element formulation to approximate the coupled system (1a)-(1c), we state its variational formulation. By multiplying the system (1a)-(1c) with test functions and applying partial integration to the stress term, we obtain

$$(\rho_{\text{ice}} H (\partial_t \mathbf{v} + f_c \mathbf{e}_z \times (\mathbf{v} - \mathbf{v}_w)), \boldsymbol{\phi})_{\Omega} = (\boldsymbol{\sigma}, \nabla \boldsymbol{\phi})_{\Omega} + (\boldsymbol{\tau}(\mathbf{v}), \boldsymbol{\phi})_{\Omega} \quad (9a)$$

$$(\partial_t A + \text{div}(A \mathbf{v}), \phi_A) = 0, \quad (9b)$$

$$(\partial_t H + \text{div}(H \mathbf{v}), \phi_H) = 0, \quad (9c)$$

where (\cdot, \cdot) is the L^2 scalar product on Ω .

3. Discretization in Space and Time.

The viscous–plastic sea-ice model is implemented in the software library Gascoigne [1]. To solve the coupled system (1a)–(1c), we follow the standard procedure in the literature and apply a splitting approach in time. First, we solve the balance laws (1b)–(1c) and then, using the updated sea-ice concentration and thickness, we compute the solution of the momentum equation. Let $0 = t^0 < t^1 < \dots < t^N = T$ be a uniform partition of $[0, T]$ with step size

$$k := t^{n+1} - t^n.$$

We set $\mathbf{v}^n = \mathbf{v}(t^n)$, $H^n = H(t^n)$, and $A^n = A(t^n)$. Then the splitting in time reads as:

1. *Transport equations:* Given \mathbf{v}^n , update (A^{n+1}, H^{n+1}) by solving the advection balances (1b)–(1c) with fixed velocity at \mathbf{v}^n .

2. *Momentum equation:* With (A^{n+1}, H^{n+1}) fixed, compute \mathbf{v}^{n+1} from the momentum equation (1a) at time t^{n+1} .

In the momentum solve, the external fields \mathbf{v}_a , \mathbf{v}_w and coefficients depending on (A, H) are evaluated at t^{n+1} . The transport equations are discretized implicitly in time using streamline diffusion. The choice is made for convenience based on the academic software library. Any other transport discretization would be possible. As the focus of the manuscript lies on the development of an efficient solving procedure for the sea-ice momentum equation, we outline the discretization of the sea-ice momentum in detail:

Discretization of the Sea-Ice Momentum Equation Owing to the stiffness of the momentum equation (1a), explicit time-stepping methods would necessitate prohibitively small time steps. Therefore, we adopt an implicit time-stepping strategy, as is standard in the literature, specifically the implicit Euler method. For the spatial discretization of the momentum equation we use a finite element discretization. Let $\{\mathcal{T}_h\}$ be a shape-regular, quasi-uniform triangulation of Ω into convex quadrilaterals K , with mesh size $h = \max_{K \in \mathcal{T}_h} \text{diam}(K)$. Using the mesh $\{\mathcal{T}_h\}$, we construct our finite element space using standard isoparametric biquadratic Lagrange elements on each quadrilateral $K \in \mathcal{T}_h$. The conforming spaces are

$$S_h := \{\phi_h \in H^1(\Omega) : \phi_h|_K \in \mathbb{Q}_2(K) \forall K \in \mathcal{T}_h\}, \quad \mathcal{V}_h := [S_h]^2, \quad \mathcal{V}_h^0 := \{\mathbf{v}_h \in \mathcal{V}_h : \mathbf{v}_h|_{\partial\Omega} = \mathbf{0}\}, \quad (10)$$

where $H^1(\Omega)$ consists of functions, defined on Ω with square-integrable derivatives. In every time step t^{n+1} , we separate the nonlinear momentum equation (9a) into an operator on the unknown, $\mathcal{A}(\mathbf{v}_h^{n+1}, \boldsymbol{\phi}_h)$, and a right-hand side, $\mathcal{F}(\boldsymbol{\phi}_h)$. We seek a \mathbf{v}_h^{n+1} such that

$$\mathcal{R}(\mathbf{v}_h^{n+1}, \boldsymbol{\phi}_h) := \mathcal{A}(\mathbf{v}_h^{n+1}, \boldsymbol{\phi}_h) - \mathcal{F}(\boldsymbol{\phi}_h) = 0, \forall \boldsymbol{\phi}_h \in \mathcal{V}_h^0, \quad (11)$$

where

$$\mathcal{A}(\mathbf{v}_h^{n+1}, \boldsymbol{\phi}_h) := (\rho_{\text{ice}} H_h^{n+1} \mathbf{v}_h^{n+1}, \boldsymbol{\phi}_h) + k(f_c \mathbf{e}_z \times \mathbf{v}_h^{n+1}, \boldsymbol{\phi}_h) + k(\boldsymbol{\sigma}^{n+1}, \nabla \boldsymbol{\phi}_h) - k(\boldsymbol{\tau}_w(t^{n+1}, \mathbf{v}_h^{n+1}, \boldsymbol{\phi}_h), \boldsymbol{\phi}_h), \quad (12)$$

$$\mathcal{F}(\boldsymbol{\phi}_h) := (\rho^n \mathbf{v}_h^n, \boldsymbol{\phi}_h) + k(\boldsymbol{\tau}_a(t^n), \boldsymbol{\phi}_h) + k(f_c \mathbf{e}_z \times \mathbf{v}_w(t^n), \boldsymbol{\phi}_h). \quad (13)$$

We solve the finite-dimensional nonlinear system of equations with a Newton-Krylov method, which is briefly outlined in the following. Let $\{\boldsymbol{\phi}_h^i\}_{i=1}^N$ be a basis of \mathcal{V}_h^0 . Then any function $\mathbf{v}_h \in \mathcal{V}_h^0$ can be represented as

$$\mathbf{v}_h = \sum_{j=1}^N v_j \boldsymbol{\phi}_h^j, \quad \mathbf{x} = (v_1, \dots, v_N)^\top \in \mathbb{R}^N.$$

We introduce the discrete residual vector $\mathbf{r} \in \mathbb{R}^N$ by $r_i := \mathcal{R}(\mathbf{v}_h^{(n+1)}, \boldsymbol{\phi}_h^i)$ for $i = 1, \dots, N$ and the right-hand side vector $\mathbf{f} \in \mathbb{R}^N$ by $f_i := \mathcal{F}(\boldsymbol{\phi}_h^i)$ for $i = 1, \dots, N$. Analogous to (11) we seek \mathbf{x}^{n+1} such that $\mathbf{r}(\mathbf{x}^{n+1}) = \mathbf{0}$. For a given iterate $\mathbf{v}_h^{(k)}$, $k = 0, 1, 2, \dots$, with coefficient vector $\mathbf{x}^{(k)}$, the Newton iteration based on the Jacobian \mathbf{J} reads

$$\mathbf{J}(\mathbf{x}^{(k)}) \delta \mathbf{x}^{(k)} = -\mathbf{r}(\mathbf{x}^{(k)}), \quad (14)$$

followed by the update

$$\mathbf{x}^{(k+1)} = \mathbf{x}^{(k)} + \alpha^{(k)} \delta \mathbf{x}^{(k)}.$$

Here $\alpha^{(k)}$ is the line search parameter. Details on the assembly of the Jacobian by the bilinear form $\mathcal{A}(\cdot, \cdot)$ (12) are given in [27]. The arising linear systems are solved by a preconditioned Krylov method (e.g. GMRES preconditioned by geometric multigrid). The procedure is described in [27]. To conclude this section, we state the solution of the coupled problem with the Newton-Krylov solve for the momentum equations in the n -th timestep.

Algorithm 1: Solution process of the momentum equation in one time step, $t_n \rightarrow t_{n+1}$.

```

1 Momentum equations: Set initial guess  $\mathbf{v}_h^{(0)} \leftarrow \mathbf{v}_h^n$  (use the solution of the previous time step  $\mathbf{v}_h^n$  as initial guess for the first step)
2 for  $k = 0, 1, 2, \dots$  until convergence do
3   Assemble residual vector  $\mathbf{r}$  with entries  $r_i := \mathcal{R}(\mathbf{v}_h, \boldsymbol{\phi}_h^i)$  for  $i = 1, \dots, N$ .
4   Assemble the Jacobian  $\mathbf{J}^{(k)}$ .
5   Solve  $\mathbf{J}(\mathbf{x}^{(k)})\delta\mathbf{x}^{(k)} = -\mathbf{r}(\mathbf{x}^{(k)})$  by GMRES with geometric multigrid preconditioning (cf. (14)).
6   Apply a line search and update  $\mathbf{v}_h^{(k+1)} \leftarrow \mathbf{v}_h^{(k)} + \alpha^{(k)}\delta\mathbf{v}_h^{(k)}$ .
7   if  $\|\mathbf{r}^{(k+1)}\| \leq \varepsilon_{\text{nl}}\|\mathbf{r}^{(0)}\|$  then
8     break
9 end
10 Accept  $\mathbf{v}_h^{n+1} \leftarrow \mathbf{v}_h^{(k+1)}$ .

```

The solving procedure described in Algorithm 1 provides the numerical solver part of the hybrid neural network-finite element method presented in this paper. The deep neural network in the hybrid method is used to improve the numerical solution after Newton convergence. We describe this process in detail in the next section.

Remark 3.1. In our implementation, we employ a *modified Newton solver* according to [27]. There, globalization of Newton's method is achieved by splitting the analytical Jacobian into a symmetric positive definite part and a remainder. By adaptively damping the remainder, robust multigrid preconditioning is preserved while ensuring convergence. For a detailed formulation we refer to [27].

4. Hybrid Neural Network-Finite Element Method

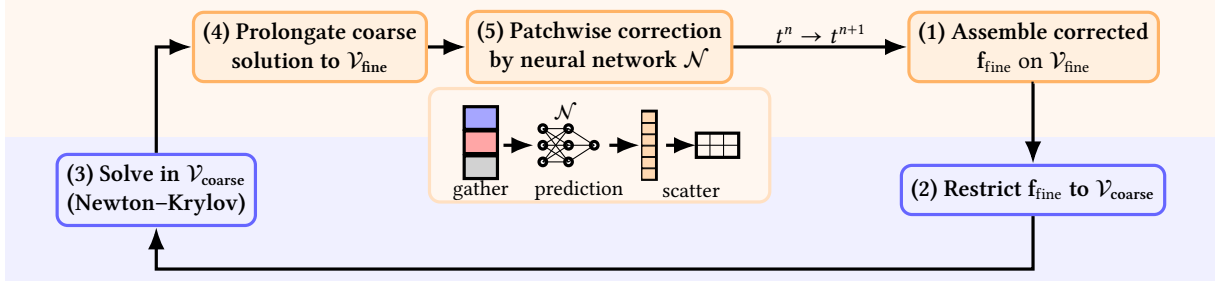


Figure 1: Compact overview of one hybrid NN-FEM time step $t^n \rightarrow t^{n+1}$: (1) use the corrected state \mathbf{v}_fine^n from the previous step to assemble the fine-space right-hand side $\mathbf{f}_\text{fine}^{n+1}$ and (2) restrict it to the working space, $\mathbf{f}_\text{coarse}^{n+1} = \mathbf{R}\mathbf{f}_\text{fine}^{n+1}$, (3) solve the sea-ice momentum equations on $\mathcal{V}_\text{coarse}$ to obtain $\mathbf{v}_\text{coarse}^{n+1}$, (4) prolongate $\mathbf{v}_\text{coarse}^{n+1}$ to the auxiliary fine space, $\mathbf{v}_\text{fine}^{n+1} = \mathbf{P}\mathbf{v}_\text{coarse}^{n+1} \in \mathcal{V}_\text{fine}$, (5) apply a patch-wise neural-network correction based on the residual and state information to compute a fine-scale increment $\delta\mathbf{v}_\text{fine}^{n+1} \in \mathcal{V}_\text{fine}$, and store the corrected fine-grid state $\mathbf{v}_\text{fine}^{n+1} = \mathbf{v}_\text{fine}^n + \delta\mathbf{v}_\text{fine}^{n+1}$ for use in assembling $\mathbf{f}_\text{fine}^{n+2}$ at the beginning of the next time step.

In the NN-FEM framework, a neural network predicts a fine-scale correction in an auxiliary space, which is applied as a post-processing step to the standard finite element discretization of the momentum equations. Our approach extends the deep neural network finite element approach proposed in [22]. Within each time step, after the Newton method of Algorithm 1 has converged, we predict fine-scale, patch-local corrections in a richer finite element space (Fig. 1), i. e. using the same finite element

space on a refined spatial mesh. This hybridization aims to improve the numerical solution without re-linearization and without solving on the finer mesh. This hybrid method is only applied to the momentum equations, the transport update remains unchanged.

The hybrid NN-FEM approach yields a separation of roles: the classical finite element method and Newton solver ensure stability and consistency on the working mesh, while the neural network provides data-driven subgrid-scale enhancement in a refined auxiliary space. The following subsections introduce the level hierarchy, notation, and transfer operators used in our hybrid algorithm.

4.1. Level Hierarchy and Notation

Let $\{\mathcal{T}_0, \dots, \mathcal{T}_L\}$ be a sequence of uniformly refined meshes for Ω , where $l = 0, \dots, L$ indicates the refinement level. Further, let \mathcal{T}_{L+S} denote a uniformly refined *auxiliary* fine mesh obtained by $S \geq 1$ refinements of \mathcal{T}_L . To each refined mesh $\mathcal{T}_h \in \{\mathcal{T}_0, \dots, \mathcal{T}_{L+S}\}$ we can relate a finite element discretization \mathcal{V}_h^0 , based on standard isoparametric biquadratic Lagrange elements, see (10). To simplify notation, we write $\mathcal{T}_{\text{coarse}}$ and $\mathcal{T}_{\text{fine}}$ for the working (coarse-resolution) and auxiliary (high-resolution) meshes of levels \mathcal{T}_L and \mathcal{T}_{L+S} , respectively, and analogously use $\mathcal{V}_{\text{coarse}}$ and $\mathcal{V}_{\text{fine}}$ for the corresponding finite element spaces \mathcal{V}_L and \mathcal{V}_{L+S} . The mesh transfer from a fine finite element space to a coarser one is accomplished with L^2 -projections, known as restrictions, and from coarse to fine ones with interpolations, known as prolongations. We write $\mathbf{P} : \mathcal{V}_{\text{coarse}} \rightarrow \mathcal{V}_{\text{fine}}$ and $\mathbf{R} : \mathcal{V}_{\text{fine}} \rightarrow \mathcal{V}_{\text{coarse}}$ for prolongation and restriction.

Remark 4.1 **On the role of Geometric Multigrid in the hybrid NN-FEM approach .** The mesh hierarchy and transfer operators, \mathbf{P} and \mathbf{R} , are readily available within the Multigrid framework. However, the Geometric Multigrid method, which used as part of the GMRES to solve the linear problems arising in each Newton iteration (see Section 3) is not a necessary part of the hybrid NN-FEM approach. Any other solver can be used to approximate the linear problem.

4.2. The Hybrid Algorithm

Algorithm 2: Hybrid neural network-finite element algorithm per time step $t^n \rightarrow t^{n+1}$

- 1 Assemble the fine-space right-hand side $\mathbf{f}_{\text{fine}}^{n+1}$ in $\mathcal{V}_{\text{fine}}$ using the stored corrected state $\mathbf{v}_{\text{fine}}^n$ from l. 8 of the previous step and restrict it to the working space: $\mathbf{f}_{\text{coarse}}^{n+1} \leftarrow \mathbf{R} \mathbf{f}_{\text{fine}}^{n+1}$.
- 2 Solve equation (11) in $\mathcal{V}_{\text{coarse}}$ with Newton-Krylov (Alg. 1) using $\mathbf{f}_{\text{coarse}}^{n+1}$ to obtain $\mathbf{v}_{\text{coarse}}^{n+1}$.
- 3 Prolongate to the auxiliary mesh: $\mathbf{v}_{\text{fine}}^{n+1} \leftarrow \mathbf{P} \mathbf{v}_{\text{coarse}}^{n+1}$.
- 4 Assemble the fine-space residual $\mathbf{r}_{\text{fine}}^{n+1}$ on $\mathcal{V}_{\text{fine}}$ for $\mathbf{v}_{\text{fine}}^{n+1}$ (cf. Alg. 1, l. 2).
- 5 Gather patch-wise inputs from $\mathbf{v}_{\text{fine}}^{n+1}$, $\mathbf{r}_{\text{fine}}^{n+1}$, and geometry information, ω , into a matrix \mathbf{X} .
- 6 Evaluate the network: $\mathbf{D} \leftarrow \mathcal{N}(\mathbf{X})$ (one row per patch).
- 7 Scatter patch outputs into the global FE coefficient vector $\delta \mathbf{v}_{\text{fine}}^{n+1}$ and update the fine-grid state $\mathbf{v}_{\text{fine}}^{n+1} \leftarrow \mathbf{v}_{\text{fine}}^{n+1} + \delta \mathbf{v}_{\text{fine}}^{n+1}$.
- 8 Store the corrected state $\mathbf{v}_{\text{fine}}^{n+1}$ for assembling $\mathbf{f}_{\text{fine}}^{n+2}$ in the next time step.

We summarize one time step of the hybrid NN-FEM correction. The overall procedure is illustrated in Fig. 1 and stated in Algorithm 2. At the beginning of time step t^{n+1} we assume that a corrected fine-grid state $\mathbf{v}_{\text{fine}}^n \in \mathcal{V}_{\text{fine}}$ from the previous step is available. The state $\mathbf{v}_{\text{fine}}^n$ is used to assemble the fine-space momentum right-hand side $\mathbf{f}_{\text{fine}}^{n+1}$, which is then restricted to the working space via

$$\mathbf{f}_{\text{coarse}}^{n+1} := \mathbf{R} \mathbf{f}_{\text{fine}}^{n+1} \quad (\text{Alg. 2, l. 1}).$$

This way, the NN-FEM update $\delta \mathbf{v}_{\text{fine}}^n$ from the previous step enters the new time step as an explicit modification of the working space right-hand side $\mathbf{f}_{\text{coarse}}^{n+1}$. All operators and the Newton-Krylov solve remain on $\mathcal{V}_{\text{coarse}}$ (see also Appendix A for notation).

With the modified working mesh right-hand side $\mathbf{f}_{\text{coarse}}^{n+1}$, we perform a Newton-Krylov solve on the working mesh (Alg. 1) to obtain the coarse solution $\mathbf{v}_{\text{coarse}}^{n+1} \in \mathcal{V}_{\text{coarse}}$. This state $\mathbf{v}_{\text{coarse}}^{n+1}$ is prolongated to the auxiliary fine space,

$$\mathbf{v}_{\text{fine}}^{n+1} := \mathbf{P} \mathbf{v}_{\text{coarse}}^{n+1} \in \mathcal{V}_{\text{fine}},$$

and we assemble the corresponding fine-space momentum residual,

$$\mathbf{r}_{\text{fine}}^{n+1} := \mathbf{r}_{\text{fine}}(\mathbf{v}_{\text{fine}}^{n+1}; \mathbf{P} \mathbf{A}^{n+1}, \mathbf{P} \mathbf{H}^{n+1}),$$

with $(\mathbf{A}^{n+1}, \mathbf{H}^{n+1})$ frozen and prolongated to $\mathcal{V}_{\text{fine}}$ (Alg. 2, l. 2–4). Next, we localize the network input data ($\mathbf{r}_{\text{fine}}^{n+1}$, $\mathbf{v}_{\text{fine}}^{n+1}$, and geometric features, ω) to overlapping patches, evaluate the neural network patch-wise, and assemble a global fine-space increment,

$$\delta \mathbf{v}_{\text{fine}}^{n+1} \in \mathcal{V}_{\text{fine}},$$

from the localized, patch-wise network outputs (Alg. 2, l. 5–7). This gather-predict-scatter pipeline respects Dirichlet boundary conditions and averages contributions at overlapping degrees of freedom (DoF). Compared to prior implementations developed in the context of the Navier-Stokes equations [23], we generalize the approach to larger patch sizes and arbitrary refinement levels between $\mathcal{V}_{\text{coarse}}$ and $\mathcal{V}_{\text{fine}}$. The corresponding operators are described in detail in Sec. 4.4. Finally, we overwrite $\mathbf{v}_{\text{fine}}^{n+1}$ with the corrected fine-grid field

$$\mathbf{v}_{\text{fine}}^{n+1} := \mathbf{v}_{\text{fine}}^{n+1} + \delta \mathbf{v}_{\text{fine}}^{n+1} \in \mathcal{V}_{\text{fine}},$$

and store $\mathbf{v}_{\text{fine}}^{n+1}$ for use in the assembly of the next fine-space right-hand side $\mathbf{f}_{\text{fine}}^{n+1}$ at the beginning of time step t^{n+2} (Alg. 2, l. 8–1). The restricted load $\mathbf{f}_{\text{coarse}}^{n+2} = \mathbf{R} \mathbf{f}_{\text{fine}}^{n+2}$ then serves as the modified working space right-hand side in the subsequent Newton-Krylov solve. Thus, the NN-FEM correction $\delta \mathbf{v}_{\text{fine}}^{n+1}$ acts as an explicit post-processing on the auxiliary fine space, $\mathcal{V}_{\text{fine}}$, that feeds back into the $\mathcal{V}_{\text{coarse}}$ problem only through the right-hand side: it does not alter the Jacobian of the Newton-Krylov iteration and does not require a fine-grid solve on $\mathcal{T}_{\text{fine}}$.

Summary of One Time Step. Given $(\mathbf{v}^n, \mathbf{A}^n, \mathbf{H}^n)$ on the coarse space $\mathcal{V}_{\text{coarse}}$ we modify the solution step for the momentum equation as follows:

1. *Momentum (Newton-Krylov on $\mathcal{V}_{\text{coarse}}$):* With $(\mathbf{A}^{n+1}, \mathbf{H}^{n+1})$ fixed and external fields evaluated at t^{n+1} , assemble the right-hand side $\mathbf{f}_{\text{fine}}^{n+1}$ using $(\mathbf{P} \mathbf{A}^{n+1}, \mathbf{P} \mathbf{H}^{n+1}, \mathbf{v}_{\text{fine}}^n)$ on $\mathcal{V}_{\text{fine}}$ and restrict to $\mathcal{V}_{\text{coarse}}$: $\mathbf{f}_{\text{coarse}}^{n+1} = \mathbf{R} \mathbf{f}_{\text{fine}}^{n+1}$. Compute $\mathbf{v}_{\text{coarse}}^{n+1}$ by solving (11) (step 2 of Alg. 2) via Alg. 1.
2. *Correction (hybrid NN-FEM):* Prolongate $\mathbf{v}_{\text{coarse}}^{n+1}$ to $\mathcal{V}_{\text{fine}}$, assemble the fine-space residual on $\mathcal{V}_{\text{fine}}$, and compute a patch-wise correction by Alg. 2 (steps 3–7). Store the corrected state $\mathbf{v}_{\text{fine}}^{n+1}$ for assembling $\mathbf{f}_{\text{coarse}}^{n+2}$ at the *beginning* of the next time step (steps 8–1 of Alg. 2).

4.3. Neural Network Inputs

Before introducing the localization and assembly operators (Sec. 4.4), we state the information passed to the network and the form of its output.

Inputs. On the auxiliary mesh $\mathcal{T}_{\text{fine}}$ (with fine space $\mathcal{V}_{\text{fine}}$), we construct, for each small local neighborhood (patch, i.e., a set of adjacent mesh elements), a fixed-length feature vector consisting of three blocks:

1. the prolongated velocity $\mathbf{P} \mathbf{v}_{\text{coarse}} = \mathbf{v}_{\text{fine}}$ restricted to the neighborhood (state);

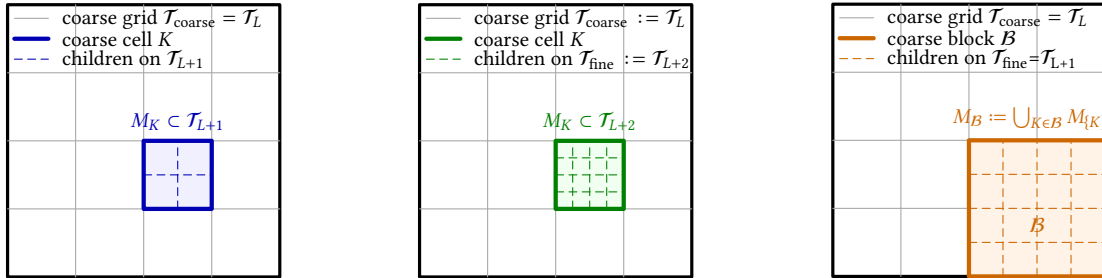
2. the corresponding entries of the momentum residual \mathbf{r}_{fine} ;
3. geometry descriptors $\boldsymbol{\omega}$ (edge lengths, aspect ratios, interior angles) of the cells in the neighborhood.

The state \mathbf{v}_{fine} encodes the local sea-ice flow, the residual encodes local error \mathbf{r}_{fine} , and the geometry block $\boldsymbol{\omega}$ adapts the map to the local cell shape.

Output and Assembly. From each local input, the network returns a velocity *correction* in the fine space, $\mathcal{V}_{\text{fine}}$. All local corrections are combined into a single fine-space correction $\delta\mathbf{v}_{\text{fine}}$ in $\mathcal{V}_{\text{fine}}$. Dirichlet values are enforced, and the result is added to \mathbf{v}_{fine} to obtain a corrected field. The concrete localization, averaging, and boundary-handling operators are detailed in Sec. 4.4.

4.4. Patch Localization of Inputs, Batched Prediction, and Global Assembly

We first localize the prolonged field \mathbf{v}_{fine} and the residual \mathbf{r}_{fine} to small patches (cf. Fig. 2). These localized quantities are used together with geometric information as the input to the network. All patches (collections of neighboring cells) are processed together in a single batched network inference to predict local velocity corrections. These local updates are then assembled into one coherent fine-grid increment, $\delta\mathbf{v}_{\text{fine}}$. In our setting, patches overlap, i.e. some degrees of freedom receive multiple predictions from the network. These duplicate predictions are averaged such that the global correction $\delta\mathbf{v}_{\text{fine}}$ lies in the fine space $\mathcal{V}_{\text{fine}}$. Boundary conditions are enforced for $\delta\mathbf{v}_{\text{fine}}$.



(a) Single-cell patch M_K ($S = 1$), (b) Single-cell patch M_K ($S = 2$), (c) Multi-cell patch M_B ($S=1$), with patch size $N_M = 0$. (a) Single-cell patch M_K ($S = 1$), (b) Single-cell patch M_K ($S = 2$), (c) Multi-cell patch M_B ($S=1$), with patch size $N_M = 1$.

Figure 2: Patch geometry and notation. Thin gray lines: coarse mesh $\mathcal{T}_{\text{coarse}}$. Dashed lines: auxiliary refinement on $\mathcal{T}_{\text{fine}}$ restricted to a patch. A single-cell patch M_K on $\mathcal{T}_{\text{coarse}}$ collects the 4^S child patches on $\mathcal{T}_{\text{fine}}$ corresponding to a single coarse cell $K \in \mathcal{T}_{\text{coarse}}$ (cf. panel (a) and panel (b)). A multi-cell patch is the union over a set of cells K , $\mathcal{B} \subset \mathcal{T}_{\text{coarse}}$ (cf. panel (c)).

For each coarse cell $K \in \mathcal{T}_{\text{coarse}}$, define its *patch* $M_K \subset \mathcal{T}_{L+S}$, $S \geq 1$, as the union of its 4^S child-patches on the auxiliary mesh $\mathcal{T}_{\text{fine}}$. The patch size N_M denotes the number of uniform coarsening steps applied to the working mesh $\mathcal{V}_{\text{coarse}}$ in order to construct the patch. Starting from the working mesh, the patch is produced by coarsening it N_M times; hence, larger values of N_M yield patches composed of fewer but correspondingly larger coarse cells. As a consequence, increasing N_M expands the local context and raises the number of degrees of freedom per patch (see Tab. 2). The case $N_M = 0$ represents the situation in which the patch consists of a single cell of the working mesh $\mathcal{V}_{\text{coarse}}$. In general, a patch of size N_M comprises 4^{N_M} cells of the working mesh $\mathcal{V}_{\text{coarse}}$. In Fig. 2 we show examples for $S = 1$ (Fig. 2a) and $S = 2$ combined with $N_M = 0$ (Fig. 2b). In Fig. 2a and Fig. 2b we show patches that consist of a single cell on the working mesh $\mathcal{V}_{\text{coarse}}$ with a patch size of $N_M = 1$. Our implementation also supports

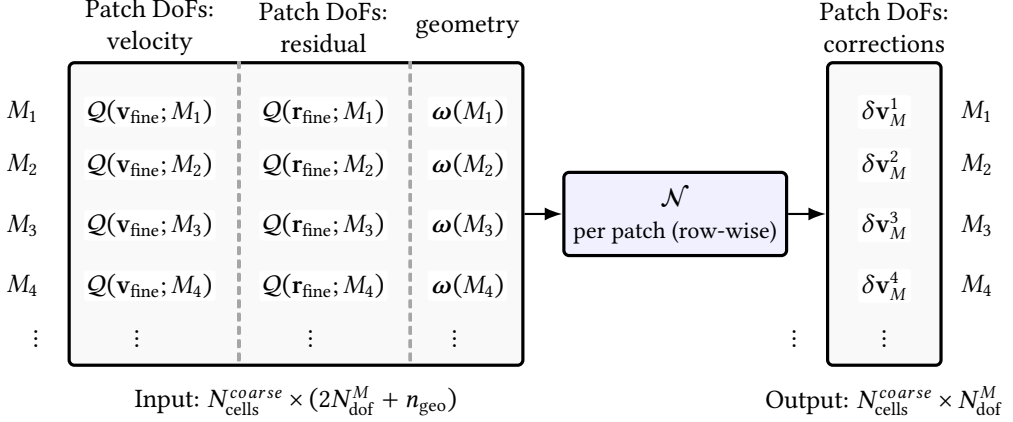


Figure 3: *Batched input matrix composed of per-patch (one patch = one row) velocity entries $Q(\mathbf{v}_{\text{fine}})$, residual entries $Q(\mathbf{r}_{\text{fine}})$, and geometric descriptors $\boldsymbol{\omega}$; the network \mathcal{N} maps each row (patch) to a vector of patch-local corrections $\delta \mathbf{v}_K^M$.*

multi-cell patches (cf. Fig. 2c). However, for clarity, we present the construction for patches based on the working mesh $\mathcal{T}_{\text{coarse}}$ (cells $K \in \mathcal{T}_{\text{coarse}}$). The extension to multi-cell patches is straightforward. Let $\mathbb{P} := \{M_K : K \in \mathcal{T}_{\text{coarse}}\}$ be the set of all patches. Denote by $N_{\text{dof}}^{\text{fine}} := \dim \mathcal{V}_{\text{fine}}$ the number of fine-grid velocity DoFs (both components), by $N_{\text{cells}}^{\text{coarse}} := |\mathcal{T}_{\text{coarse}}|$ the number of patches, and by N_{dof}^M the number of velocity DoFs supported on a single patch.

Gather. The goal of the gather step is to convert global fine-space vectors into a batched, row-wise layout (one row per patch) for efficient, vectorized network inference. For each patch $M_K \in \mathbb{P}$, let $\pi_K : \{1, \dots, N_{\text{dof}}^M\} \rightarrow \{1, \dots, N_{\text{dof}}^{\text{fine}}\}$ be the local-to-global DoF map on M_K , and define the *selection* matrix $G_K \in \{0, 1\}^{N_{\text{dof}}^M \times N_{\text{dof}}^{\text{fine}}}$ by $(G_K)_{j,i} = 1$ iff $i = \pi_K(j)$, else 0. Then, for any fine-grid coefficient vector $\mathbf{x}^{\text{fine}} \in \mathbb{R}^{N_{\text{dof}}^{\text{fine}}}$, the patch vector is

$$q_K = G_K \mathbf{x}^{\text{fine}} \in \mathbb{R}^{N_{\text{dof}}^M}.$$

Stacking one row per patch gives the *batched* (row-wise) layout

$$Q(\mathbf{x}^{\text{fine}}) = \begin{bmatrix} G_1 \\ \vdots \\ G_{N_{\text{cells}}^c} \end{bmatrix} \mathbf{x}^{\text{fine}} \in \mathbb{R}^{N_{\text{cells}}^{\text{coarse}} \times N_{\text{dof}}^M}. \quad (15)$$

The matrices G_K are fixed, extremely sparse, and can be stored as index lists.

Network Input. Let $\mathbf{v}_{\text{fine}} = \mathbf{P} \mathbf{v}_{\text{coarse}}$ be the prolongated velocity and let \mathbf{r}_{fine} be the fine-grid momentum residual. For each patch, we *gather* the local coefficients of \mathbf{v}_{fine} and \mathbf{r}_{fine} into a row and append the geometric patch descriptors $\boldsymbol{\omega}$. Stacking all rows gives

$$\mathbf{X} = [Q(\mathbf{v}_{\text{fine}}) \mid Q(\mathbf{r}_{\text{fine}}) \mid \boldsymbol{\omega}] \in \mathbb{R}^{N_{\text{cells}}^{\text{coarse}} \times (2N_{\text{dof}}^M + n_{\text{geo}})}. \quad (16)$$

Here the three blocks are, per row (i.e. per patch): local velocity DoFs, local residual DoFs, and n_{geo} geometric features. For a given patch M_B with prediction jump S , the flattened row dimension equals the network input size $N_{\text{in}} = 2N_{\text{dof}}^M + n_{\text{geo}}$, and the patch correction has length $N_{\text{out}} = N_{\text{dof}}^M$; concrete values for $(N_{\text{in}}, N_{\text{out}})$ across (M, S) are listed in Tab. 2.

Patch-wise Prediction. The patch network \mathcal{N} acts *row-wise* on \mathbf{X} , producing one correction vector per patch:

$$\mathbf{D} = \mathcal{N}(\mathbf{X}) \in \mathbb{R}^{N_{\text{cells}}^{\text{coarse}} \times N_{\text{dof}}^M},$$

where the K -th row $\mathbf{D}_{K,:}$ is the patch-local velocity correction $\delta\mathbf{v}^{M_K} \in \mathbb{R}^{N_{\text{dof}}^M}$ for M_K .

Scatter. Patch predictions must be merged into one fine-space update and made compatible with Dirichlet boundary conditions. Using the gather matrices $G_K \in \{0, 1\}^{N_{\text{dof}}^M \times N_{\text{dof}}^{\text{fine}}}$ from above, define the *scatter* matrices $S_K := G_K^\top \in \{0, 1\}^{N_{\text{dof}}^{\text{fine}} \times N_{\text{dof}}^M}$, which add a patch vector back into the global layout. Let $W = \text{diag}(\mu_1, \dots, \mu_{N_{\text{fine}}})$ be diagonal *partition-of-unity weights* chosen so that $W \sum_K S_K G_K = I$ on interior DoFs, and let $B = \text{diag}(\beta_1, \dots, \beta_{N_{\text{fine}}})$ with $\beta_i = 0$ on Dirichlet DoFs and $\beta_i = 1$ otherwise. The fine-grid increment assembled from all patches is

$$\delta\mathbf{v}_{\text{fine}} = BW \sum_{K=1}^{N_{\text{cells}}^{\text{coarse}}} S_K \delta\mathbf{v}_K^M = BW \sum_{K=1}^{N_{\text{cells}}^{\text{coarse}}} S_K \mathbf{D}_{K,:}^\top \in \mathbb{R}^{N_{\text{fine}}^{\text{fine}}}. \quad (17)$$

By construction, $\sum_K S_K G_K$ is diagonal with entries equal to the local patch multiplicities; hence on interior DoFs, $W \sum_K S_K G_K = I$, and $BW \sum_K S_K G_K = B$ overall. Thus, W averages overlapping predictions of the network, and B enforces homogeneous Dirichlet values.

4.5. Neural network

We train the network \mathcal{N} in a supervised setting with targets from fine-space reference simulations, $\mathbf{v}_{\text{ref}}^{\text{fine}}$, with converged Newton-Krylov iterations. For each of these snapshots we build, in $\mathcal{V}_{\text{fine}}$, the patch-wise inputs (state, \mathbf{v}_{fine} , residual, \mathbf{r}_{fine} , geometry, ω) and the corresponding target, the *corrections* to the coarse solution obtained from a fine reference solve. Concretely, the target on the patch M_B is the local difference between the reference velocity and the prolonged solution $\mathbf{v}_{\text{fine}} = \mathbf{P}\mathbf{v}_{\text{coarse}}$, restricted to that patch.

Training samples are the rows of the batched input matrix, collected over all patches and all snapshots. Mini-batches are formed by randomly sampling rows across snapshots. The loss is the mean-squared error over patches. We proceed to a formal specification of the network architecture, targets and loss, together with the optimization details.

Neural Network Architecture In the hybrid NN-FEM approach we use a compact multilayer perceptron (MLP) that maps the patch-wise input vector $\mathbf{x} \in \mathbb{R}^{N_{\text{in}}}$ to a local velocity correction $\mathcal{N}(\mathbf{x}) \in \mathbb{R}^{N_{\text{out}}}$. The network has ℓ layers and is defined as follows. We set

$$\mathbf{h}^{(0)} = \mathbf{x} \quad \text{and} \quad \mathbf{h}^{(i)} = \sigma(\mathbf{W}_i \mathbf{h}^{(i-1)} + \mathbf{b}_i), \quad i = 1, \dots, \ell - 1.$$

Here $\mathbf{W}_i \in \mathbb{R}^{w \times d_{i-1}}$, $\mathbf{b}_i \in \mathbb{R}^w$, $d_0 = N_{\text{in}}$, and $d_i = w$ for $i = 1, \dots, \ell - 1$. The output layer is

$$\mathcal{N}(\mathbf{x}) = \mathbf{W}_\ell \mathbf{h}^{(\ell-1)} + \mathbf{b}_\ell, \quad \mathbf{W}_\ell \in \mathbb{R}^{N_{\text{out}} \times w}, \quad \mathbf{b}_\ell \in \mathbb{R}^{N_{\text{out}}}.$$

Where dimensions match, we use a residual connection

$$\mathbf{h}^{(i)} \leftarrow \mathbf{h}^{(i)} + \mathbf{h}^{(i-1)}.$$

In our implementation we choose the activation function $\sigma = \tanh$ and apply layer normalization to the pre-activations,

$$\mathbf{h}^{(i)} = \sigma(\text{LN}_i(W_i \mathbf{h}^{(i-1)} + b_i)),$$

which we have found to yield the most stable results.

Targets and Loss. For a fine reference solution $\mathbf{v}_{\text{fine}}^{\text{ref}}$, which is a computed on a mesh with higher resolution without deep neural network, and patch M_K , we define the per-patch target increment $\mathbf{y}_M^K := G_K(\mathbf{v}_{\text{fine}}^{\text{ref}} - \mathcal{P}\mathbf{v}_{\text{coarse}}) \in \mathbb{R}^{N_{\text{dof}}^M}$. Let $\delta\mathbf{v}_M^K \in \mathbb{R}^{N_{\text{dof}}^M}$ denote the network's prediction for patch M_K . A simple mean-squared error with weight decay is

$$\mathcal{L}(\theta) = \frac{1}{|\mathcal{S}|} \sum_{s \in \mathcal{S}} \frac{1}{N_{\text{cells}}^{(s)}} \sum_{K=1}^{N_{\text{cells}}^{(s)}} \|\delta\mathbf{v}_M^{K,(s)} - \mathbf{y}_M^{K,(s)}\|_2^2 + \alpha \|\theta\|_2^2, \quad (18)$$

where \mathcal{S} indexes training snapshots and $\alpha > 0$ is the Tikhonov/weight-decay parameter.

Optimization Details. For the training, we use the AdamW optimizer [20] (learning rate 10^{-4} , batch size 64), which leads to better stability compared to alternatives, as we observed in [23]. We use Tikhonov regularization with a scaling factor $\alpha = 10^{-3}$. The training is run for 40 epochs. Then, the model with the lowest validation loss is selected. For stable training, we use a warm-up with a low initial learning rate and a cyclical scheduler performing a single cycle over all epochs [32]. Network parameters are initialized with PyTorch's default initialization.

We conclude this section with a few remarks on the network design and implementation aspects of the neural network.

Remark 4.2 Impact of the correction on Newton's method . In the sense of inexact Newton [4, 6], the NN-FEM correction $\delta\mathbf{v}_{\text{fine}}^n$ at t^n induces an *additive right-hand-side perturbation* of the residual $\mathcal{R}_{\text{coarse}}^{n+1}$ at t^{n+1} , with the same Jacobian since the perturbation depends on $\mathbf{v}_{\text{fine}}^n$ and is independent of $\mathbf{v}_{\text{coarse}}^{n+1}$. Thus, the local assumptions for inexact Newton (invertibility and Lipschitz continuity of \mathcal{J}) can be transferred, and the theory can be applied here. Admissibility then reduces to a *relative smallness* of the additive load at the initial guess, as detailed in Remark A.1. In particular, the local Newton convergence region is preserved up to a small factor. A refined treatment and detailed theoretical investigation is left to future work. Next, we explain how we design the neural network such that the *relative smallness* assumption can be fulfilled (cf. (19)). We note that this reasoning is rather heuristic and will be investigated empirically through ablation studies in Sec. 5.4.

Remark 4.3 Neural network design for stability . To ensure the convergence of the nonlinear solver, the perturbation of the fine-level right-hand side $\mathbf{f}_{\text{fine}}^{n+1}$, induced by $\delta\mathbf{v}_{\text{fine}}^n$, must be bounded in terms of the unperturbed residual (cf. Remark A.1). We therefore hypothesize that the neural network should exhibit two key properties: *state-awareness*, \mathbf{v}_{fine} , and *residual-awareness*, \mathbf{r}_{fine} . We achieve this by explicitly including both, the current state and residual information, as inputs to the network.

State-awareness requires that the correction $\delta\mathbf{v}_{\text{fine}}$ aligns with the local solution structure. State-awareness is provided by feeding local patches of the velocity field $\mathcal{P}\mathbf{v}_{\text{coarse}}$ to the network. This allows the correction $\delta\mathbf{v}_{\text{fine}}$ to align with the local solution geometry and stress state, ensuring consistency with the Jacobian structure $\mathcal{J}(\mathbf{v}_{\text{coarse}})$ and preventing the introduction of spurious modes.

Residual-awareness requires that the correction magnitude is appropriately scaled relative to the local discretization error, thereby controlling the perturbation of $\mathbf{f}_{\text{coarse}}$ through the corrected solution \mathbf{v}_{fine} to satisfy the bound above. Residual-awareness is provided by including the local residual $\mathcal{R}(\mathbf{v}_{\text{coarse}}; \cdot)$ as an additional input feature (cf. (11)).

Remark 4.4 Parallelism, batching, and conservation . Gather \mathcal{Q} , prediction \mathcal{N} , and scatter operations are embarrassingly parallel across patches: patch-wise predictions are mutually independent up to the scatter step. In practice, all patch-local data are stacked into a single input array so that \mathcal{N} can be evaluated in one batched call on modern accelerators, yielding higher arithmetic intensity than the

typically memory-bound finite element kernels and thus higher throughput. Boundary values are preserved by zeroing Dirichlet DoFs via the scatter mask B , and partition-of-unity weights W stabilize the assembly by averaging contributions at shared DoFs in (17). Consequently, the global correction avoids spurious jumps at patch interfaces.

5. Numerical Experiments

In this section, we describe the numerical experiments performed to generate training data, train neural networks, and test the NN-FEM algorithm for sea-ice simulations. The experiments involve several parameter and ablation studies. The experiments ran on a workstation with two Intel Xeon E5-2640 v4 CPUs, 756 GB RAM, and an NVIDIA Tesla V100 GPU. The numerical solver, which is part of Gascoigne3D [1], runs on the CPU, while the network is evaluated on the GPU using the libtorch library [28]. The neural network architecture is a simple MLP with recurrent connections. While more advanced architectures are supported, the MLP performed reliably in previous works [23]. In Section 5.1 we introduce the benchmark setup. Section 5.2 outlines the training data and introduces the metrics for evaluation of the benchmark problem. In the experiments we conduct in Section 5.3, we investigate how key parameters of the algorithm, namely the patch size, N_M , the number of predicted levels, S , and the choice of network inputs, affect accuracy and generalization. Rather than optimizing the network architecture, we conduct a systematic study to understand the influence of the aforementioned parameters on the performance of the NN-FEM approach.

5.1. Benchmark Setup

We solve the sea-ice dynamics (1a)–(1c) for the benchmark described in [25]. We consider a square domain $\Omega = (0, 512 \text{ km})^2$, initially covered by a thin, motionless layer of sea-ice. The initial conditions are

$$\mathbf{v}(\mathbf{x}, 0) = \mathbf{0}, \text{ m s}^{-1}, \quad A(\mathbf{x}, 0) = 1, \quad H(\mathbf{x}, 0) = 0.3 \text{ m}.$$

A cyclone propagates from the center of the domain toward the upper-right corner (northwest direction), while the ocean current is prescribed to circulate counterclockwise. The corresponding wind and ocean velocities in (2) are specified as

$$\begin{aligned} \mathbf{v}_w(\mathbf{x}, t) &= 0.01 \text{ m s}^{-1} \begin{pmatrix} -1 + 2y/(512 \text{ km}) \\ 1 - 2x/(512 \text{ km}) \end{pmatrix}, \\ \mathbf{v}_a(\mathbf{x}, t) &= \omega(\mathbf{x}) \bar{\mathbf{v}}_a^{\max} \begin{pmatrix} \cos(\alpha) & \sin(\alpha) \\ -\sin(\alpha) & \cos(\alpha) \end{pmatrix} \begin{pmatrix} x - m_x(t) \\ y - m_y(t) \end{pmatrix}, \end{aligned}$$

where

$$\begin{aligned} \bar{\mathbf{v}}_a^{\max} &= \bar{\mathbf{v}}_a^{\max}(t) = 15 \text{ m s}^{-1} \begin{cases} -\tanh((4-t)(4+t)/2) & t \in [0 \text{ d}, 4 \text{ d}] \\ \tanh((12-t)(-4+t)/2) & t \in [4 \text{ d}, 8 \text{ d}] \end{cases}, \\ \alpha &= \alpha(t) = \begin{cases} 72^\circ & t \in [0 \text{ d}, 4 \text{ d}] \\ 81^\circ & t \in [4 \text{ d}, 8 \text{ d}] \end{cases}, \\ m_x(t) &= m_y(t) = \begin{cases} 256 \text{ km} + 51.2 \text{ km d}^{-1} t & t \in [0 \text{ d}, 4 \text{ d}] \\ 665.6 \text{ km} - 51.2 \text{ km d}^{-1} t & t \in [4 \text{ d}, 8 \text{ d}] \end{cases} \\ \omega(\mathbf{x}) &= \omega(\mathbf{x}, t) = \frac{1}{50} \exp \left(-\frac{\sqrt{(x - m_x(t))^2 + (y - m_y(t))^2}}{100 \text{ km}} \right). \end{aligned}$$

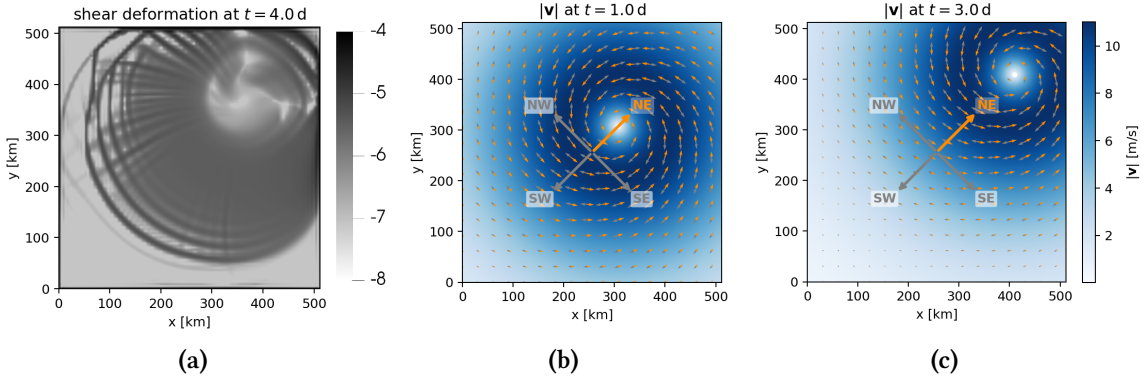


Figure 4: *Test and training setups. For training the model we consider the sea-ice benchmark problem defined in [25], where a cyclone is moving in northeast direction over an ice-covered domain. Panel (a) shows sea-ice shear deformation after 4 days of simulation. Panel (b) and (c) indicates the wind field of the cyclone v_w at $t = 1 \text{ d}$ and $t = 3 \text{ d}$, respectively. For testing the network the wind field are either anti-cyclone or cyclone moving in north-west (NW), south-west (SW) or south-east (SE) direction. The different directions are indicated in gray in panel b and c.*

5.2. Neural Network Parameters, Training and Metrics for Evaluation

For training and testing, we vary configuration parameters that, on the one hand, modify the benchmark problem itself, such as

1. *Wind-field direction:* north-west, north-east, south-east, or south-west;
2. *Direction of rotation:* cyclone or anticyclone.

A visualization of these configurations is provided in Fig. 4. We note that, for the rotated wind forcing, the predicted fields align with the north-east reference up to rotation, indicating approximate rotational equivariance despite the local, patch-wise design. On the other hand, we vary parameters that affect the network input and output dimensions, including

3. *Auxiliary refinement depth S :* the number of uniform refinements used to define the auxiliary space V_{fine} from the working space V_{coarse} (cf. Sec. 4); (a larger S results in a finer V_{fine});
4. *Patch size N_M :* the number of uniform coarsening steps used to construct the patch from the working mesh.

We collect these parameters in Tab. 1 and list the corresponding input and output sizes ($N_{\text{in}}, N_{\text{out}}$) per patch size N_M and mesh refinement level S in Tab. 2. We use the benchmark setting described in Section 5.1 to generate training data separately for each pair (N_M, S) . We neglect the first 30 time steps and obtain 66 snapshots. The training data are split into two sets: 75% for training and 25% for testing. The remaining settings (other wind directions and anticyclones) are used for validation.

The neural network architecture is a simple MLP with recurrent connections. While more advanced architectures are supported, the MLP performed reliably in previous works [23]. Further, the focus of this work is to formulate a hybrid NN-FE method, based on DNN-MG [23, 22, 21], for coupled problems. In the experiments we conduct in this section, we investigate how key parameters of the algorithm, namely the patch size, the number of predicted levels, and the choice of network inputs, affect accuracy and generalization. Rather than optimizing the network architecture, we conduct a systematic study to understand the influence of the aforementioned parameters on the performance of the NN-FEM approach.

Evaluation Metrics. Unless stated otherwise, all quality metrics are computed in the auxiliary fine space $\mathcal{V}_{\text{fine}}$. Given the corrected field \mathbf{v}_{fine} and the fine reference $\mathbf{v}_{\text{fine}}^{\text{ref}}$,

(M1) *Discrete ℓ^2 error:* $E_{\ell^2} := \|\mathbf{v}_{\text{fine}} - \mathbf{v}_{\text{fine}}^{\text{ref}}\| = \left((\mathbf{v}_{\text{fine}} - \mathbf{v}_{\text{fine}}^{\text{ref}})^{\top} (\mathbf{v}_{\text{fine}} - \mathbf{v}_{\text{fine}}^{\text{ref}}) \right)^{1/2}$. Here $\mathbf{v}_{\text{fine}}^{\text{ref}}$ denotes the solution at 2 km resolution.

(M2) *LKF count:* We detect linear kinematic features (LKFs) on the coarse mesh as described in [14]. The detection algorithm is based on the shear deformation,

$$\dot{\epsilon}_{\text{shear}} = \sqrt{(\dot{\epsilon}_{11} - \dot{\epsilon}_{22})^2 + 4 \dot{\epsilon}_{12}^2},$$

where ϵ_{ij} denote the components of the symmetric strain-rate tensor (3). The shear deformation, and thus the LKF detection, are computed on the coarse mesh. In accordance with the hybrid NN-FEM concept, only the neural network operates on the fine level, while the quantities of interest are evaluated on the coarse resolution. All parameters in the detection algorithm are kept constant across all experiments so that the number of LKFs, N_{LKF} , is comparable between settings.

(M3) *Solver effort:* total Newton iterations $N_{\text{Newton}} := \sum_n \kappa_n$, with κ_n the iterations in the momentum solve at time step n .

(M4) *Wall time:* Solution time for the momentum equation, T_{mom} , and its decomposition into Newton-Krylov time T_{NK} , CPU to GPU copy time T_{cpy} , and network inference time T_{nn} .

Unless stated otherwise, the metrics (M1)–(M4) are reported as arithmetic means over all test cases, all wind directions and both cyclones and anticyclones. We do not average across jump levels S or patch sizes N_M ; results for each S and N_M are always reported separately. Accuracy is quantified by E_{ℓ^2} and N_{LKF} ; efficiency by N_{Newton} and T_{mom} .

Table 1: Parameters of the hybrid neural network-finite element method. We use a multilayer perceptron with width w and number of network layers (depth) l , and test different patch configurations by varying the additional refinements of the mesh S and patch size N_M .

Width w	Layers l	Jump level S (finer $\mathcal{V}_{\text{fine}}$)	Patch size N_M
{128, 256, 512}	{2, 4, 8}	{1, 2}	{0, 1, 2}

5.3. Impact of Patch Size, Predicted Levels and Network Parameters

We study how the *patch size* (collection of neighboring mesh cells), N_M , the *prediction jump* S (which controls the number of degrees of freedom in the auxiliary space $\mathcal{V}_{\text{fine}}$), and the *network depth and width* (l, w) affect the performance of the hybrid NN-FEM method with respect to simulate LKFs. We vary $N_M \in \{0, 1, 2\}$, $S \in \{1, 2\}$, and $l \in \{2, 4, 8\}$, $w \in \{128, 256, 512\}$, see Tab. 1. Accuracy and efficiency are quantified by the metrics (M1)–(M4). In the following we evaluate the simulated shear deformation qualitatively by visual comparison (Section 5.3.1). Accuracy of the NN-FEM is addressed by deriving the error E_{ℓ^2} between the NN-corrected solution and the high-resolution reference (M1) combined with an analysis of the number of LKFs N_{LKF} (M2) (Section 5.3.2). The Newton-iterations (M3) and the run time (M4) required for simulations with the NN-FEM are evaluated in Section 5.3.3. The main findings are summarized in Section 5.3.4.

5.3.1. Comparison of shear deformation fields.

Single-level prediction ($S = 1$). We first assess accuracy for single-level prediction, where the NN is trained on a 4 km mesh ($S = 1$) and used to correct simulations on the 8 km working mesh. We exemplarily visualize the NN-FEM simulations for an anti-cyclone setting with northwest wind direction. All

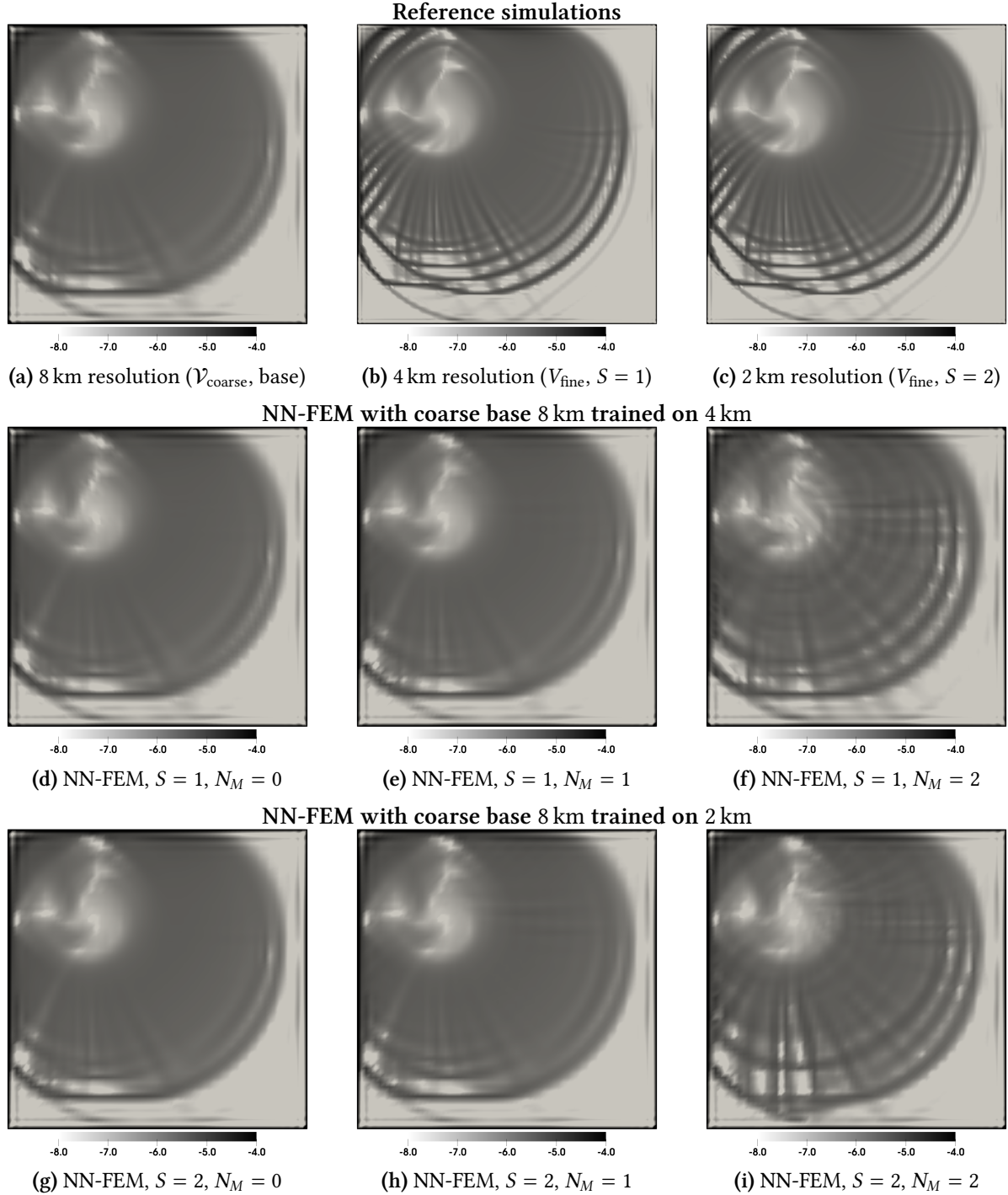


Figure 5: Shear deformation simulated with the benchmark setup, where the direction of the cyclone is changed to north-west. The top row shows the simulations performed without NN: (a) 8 km coarse resolution simulation, (b) 4 km reference simulation, the target for NN-FEM with $S = 1$, (c) 2 km reference simulation, the target for NN-FEM with $S = 2$. The middle and bottom rows show the simulated shear deformation derived from a NN-FEM simulation on $\mathcal{V}_{\text{coarse}}$ with a mesh size of 8 km. The corresponding NN uses varying patch size N_M and operates on $\mathcal{V}_{\text{fine}}$ with mesh sizes of 4 km, i.e. $S = 1$ (middle row) and 2 km, i.e. $S = 2$ (bottom row).

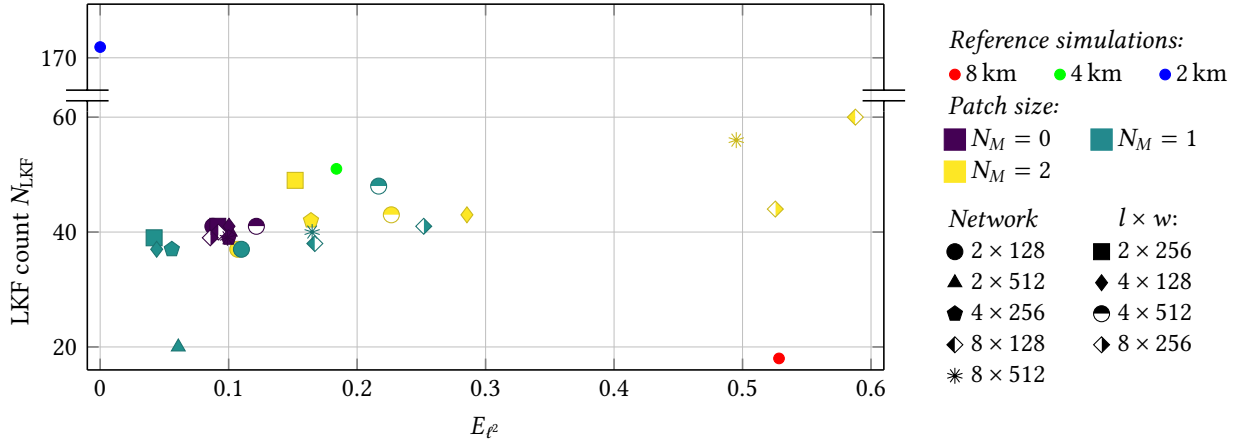


Figure 6: Scatter plot with the error E_{ℓ^2} between the reference solution, $\mathbf{v}_{\text{fine}}^{\text{ref}}$, and the corrected network solution, \mathbf{v}_{fine} , over the number of LKFs (cf. (M1), (M2)) under varying patch sizes ($N_M \in \{0, 1, 2\}$; in purple, green and yellow, respectively) and for different depth and width, $l \times w$, of the network indicated by markers. The jump level is set to $S = 2$. The red, blue and green dot indicates the number of LKFs detected from the reference solutions (without NN) on the meshes with side length 8 km, 4 km and 2 km, respectively. All combinations are able to offer a reasonable trade-off between accuracy with respect to the reference solution and the number of LKFs.

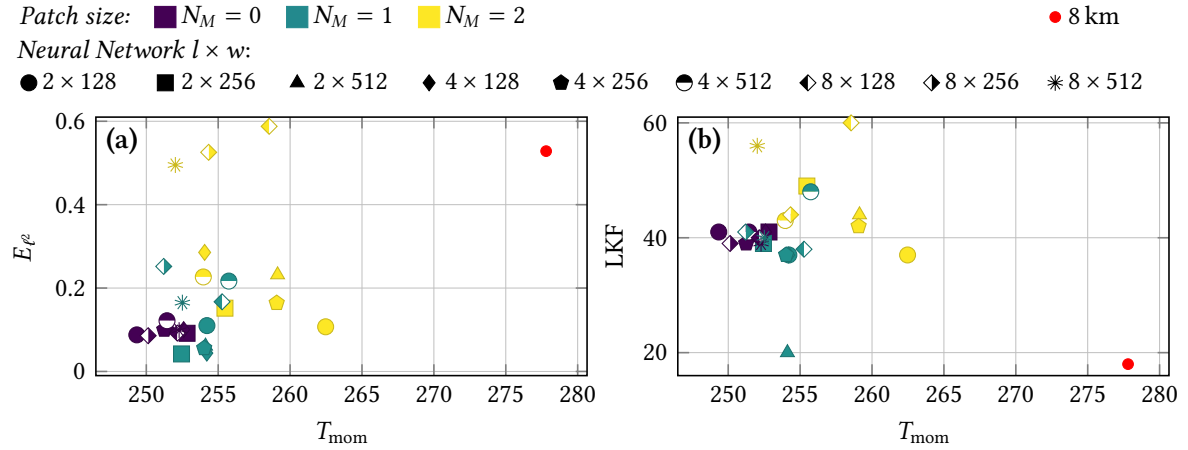


Figure 7: Scatter plot with time to solution to solve the sea-ice momentum equation for varying patch sizes ($N_M \in \{0, 1, 2\}$; in purple, green and yellow, respectively) and for different network configurations analogous to Fig. 6. The time is presented with respect to (a) the error E_{ℓ^2} between the reference solution with 2 km resolution and the corrected network solution, and (b) LKF count, N_{LKF} . Solving the sea-ice momentum without NN requires T_{mom} : 277 s, 2751 s, 29 656 s, at 8 km, 4 km and 2 km resolution, respectively.

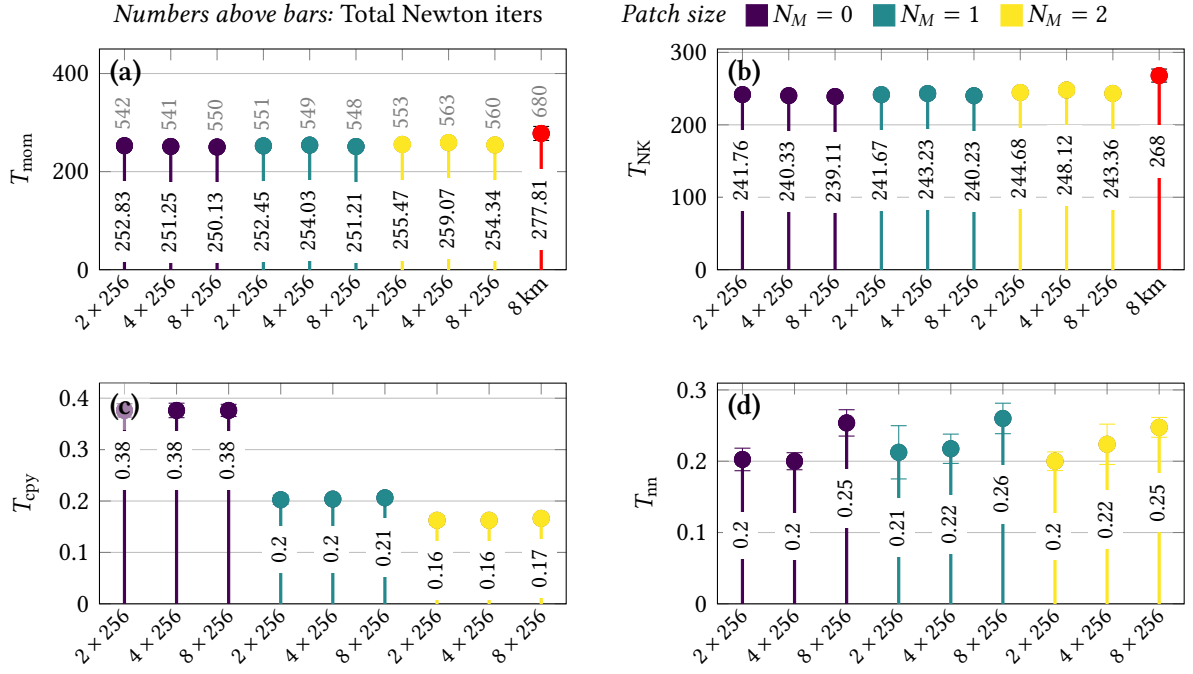


Figure 8: Timing of NN-FEM approach across patch sizes with respect to the sea-ice momentum solve, Newton-Krylov solver time, host-device copy time, and network inference time. The run times are presented for varying patch sizes $N_M \in \{0, 1, 2\}$ (colored purple, green and yellow, respectively), different network widths and depths (presented on the horizontal axis). Numbers above bars in panel (a) (colored in gray) denote total Newton iterations N_{Newton} . The red 8 km label in panel (a) and (b) denotes the solution at 8 km grid resolution without NN-FEM corrections. On a mesh with side length of 4 km and 2 km, the run time without NN-FEM is 2751 s, 29 656 s, respectively.

Table 2: Input and output sizes N_{in} , N_{out} of the neural network for different patch sizes N_M and additional mesh refinements S (the larger S the more degree of freedom contains $\mathcal{V}_{\text{fine}}$). Here, n_M denotes the number of DoFs per component and per patch on the auxiliary (refined) level. The input dimension is $N_{\text{in}} = 4n_M + 8$, corresponding to 2 momentum components, 2 residual components, and 8 geometric features. The output dimension is $N_{\text{out}} = 2n_M$, corresponding to the 2 momentum components.

N_M	$S = 1$			$S = 2$		
	n_M	N_{in}	N_{out}	n_M	N_{in}	N_{out}
0	25	108	50	81	332	162
1	81	332	162	289	1164	578
2	289	1164	578	1089	4364	2178

other setups perform qualitatively similar. In Fig. 5d–5f we show the NN-corrected fields on the 8 km resolution grid for $N_M \in \{0, 1, 2\}$. These are compared with the 8 km baseline without NN (Fig. 5a) and the 4 km target (Fig. 5b). The visual comparison shows that increasing N_M systematically improves the approximation relative to the baseline. We summarize the observations for each patch size:

$N_M = 0$: The smallest patch setting (Fig. 5d) stays close to the 8 km baseline (Fig. 5a); the influence of the network correction on the simulated shear deformation is barely visible.

$N_M = 1$: Compared to $N_M = 0$, the larger patch size visually improves the agreement with the 4 km reference (Fig. 5e).

$N_M = 2$: The setting (Fig. 5f) approaches the 4 km target (Fig. 5b) even better than $N_M = 1$. Larger patches provide more sharply defined features and enable richer corrections compared to the baseline.

Two-level prediction ($S = 2$). We now consider two-level prediction with $S = 2$, where the NN is trained on a 2 km mesh and used to correct the 8 km working mesh. Fig. 5g–5i shows snapshots of the NN-FEM solution for $N_M \in \{0, 1, 2\}$. We compare these to the 8 km baseline without NN (Fig. 5a) and the 2 km target (Fig. 5c). For larger N_M , we obtain approximations that are qualitatively similar to a 4 km resolution (cf. Fig. 5b), even though the corrections are formed on the 2 km auxiliary grid. For fixed N_M , raising the jump level from $S = 1$ to $S = 2$ yields higher LKF counts across the tested setups (Fig. 5i, Tab. 3(d)–3(f)). We did not observe patch-boundary artifacts in the analyzed cases. The auxiliary space $\mathcal{V}_{\text{fine}}$ constructed on a 2 km grid allows the patch corrections to represent higher spatial frequencies than those obtained from an auxiliary space defined on a 4 km grid. Comparing the second and third rows of Fig. 5 and Tab. 3(a)–3(c) with Tab. 3(d)–3(f) shows that $S = 2$ yields a qualitative improvement over $S = 1$. Therefore, we focus on $S = 2$ in what follows.

Remark 5.1 NN-FEM approach on large patches . We exclude the results for $N_M = 3$ combined with $S = 1, 2$, as the network corrections produce numerous spurious high-frequency artifacts. A plausible explanation is data scarcity relative to the input and parameter dimension: as N_M increases, the feature dimension grows while the number of statistically independent patches per snapshot decreases, worsening the sample-to-parameter ratio. With substantially larger training datasets, $N_M = 3$ could become advantageous; however, under the current data volume it leads to noisy predictions.

5.3.2. Metric (M1) and (M2): Accuracy and LKF Counts

Tab. 3 summarizes the LKF counts obtained from simulations on the 8 km mesh corrected with the NN-FEM approach for different patch sizes $N_M \in \{0, 1, 2\}$ and jump levels $S \in \{1, 2\}$. Increasing N_M increases the number of resolved LKFs across architectures, while changes in network depth and width (l, w) shift the absolute counts only slightly. In Fig. 6 we plot the error E_{ℓ} versus the number of LKFs

Table 3: LKF counts evaluated from simulations on the 8 km mesh corrected with the NN-FEM approach using patch sizes $N_M \in \{0, 1, 2\}$ and trained on refined meshes corresponding to 4 km and 2 km resolution ($S \in \{1, 2\}$, respectively). Increasing N_M increases the number of resolved LKFs across architectures. Network depth and width (l, w) shifts absolute counts only slightly compared to a change in the patch size. Solving the sea-ice momentum without NN results in an LKF count of 18, 51, 171, at 8 km, 4 km and 2 km resolution, respectively.

		$N_M = 0, S = 1$			$N_M = 1, S = 1$			$N_M = 2, S = 1$			LKFs	
		w	l	2	4	8	w	l	2	4	8	
		128		37	37	37	128		36	35	35	
		256		36	35	36	256		36	34	35	
		512		36	37	35	512		22	36	37	
		$N_M = 0, S = 2$			$N_M = 1, S = 2$			$N_M = 2, S = 2$				
		w	l	2	4	8	w	l	2	4	8	
		128		41	41	40	128		37	37	38	128
		256		41	39	39	256		39	37	41	256
		512		40	41	39	512		20	48	40	512
		$N_M = 0, S = 2$			$N_M = 1, S = 2$			$N_M = 2, S = 2$				
		w	l	2	4	8	w	l	2	4	8	
		128		37	43	60	128		37	43	60	128
		256		49	42	44	256		49	42	44	256
		512		44	43	56	512		44	43	56	512

N_{LKF} for $S = 2$. All combinations achieve a reasonable trade-off between accuracy and additional LKF features under varying patch sizes and architectures. The patch size is the dominant factor, whereas the architecture modulates the absolute counts without changing the ranking (Tab. 3a–3f).

For $S = 2$ we can resolve the effect of N_M and (l, w) in more detail:

$N_M = 0$: In terms of LKFs the NN-FEM approach yields a moderate increase over the baseline count of 18 LKFs (Tab. 3). The model size cannot compensate for the limited local context, but this configuration provides a low-cost baseline when memory is constrained.

$N_M = 1$: The $l = 2, w = 256$ model is competitive, but higher-capacity networks are advantageous. A model with $l = 4$ and $w = 512$ performs best in terms of LKFs (Tab. 3), and a model with $l = 8$ and $w = 256$ exhibits similar LKF counts. The larger number of training patches for $N_M = 1$ supports stable training of the larger networks and compensates for the reduced context. This choice offers a good runtime/accuracy trade-off and was consistent across the tested scenarios.

$N_M = 2$: A compact model with $l = 2, w = 256$ strikes a favorable error-LKF balance (Fig. 6). Deeper or wider variants show no systematic gains (Tab. 3f).

Among the tested settings, $N_M = 2$ was most favorable in our configuration. Overall, hybrid NN-FEM on the 8 km grid substantially increases N_{LKF} compared to the 8 km baseline, approaching the 4 km reference with 51 detected LKFs. (Fig. 6, Tab. 3). At 2 km resolution, the reference field contains 171 LKFs, i.e., more than three times the best hybrid NN-FEM counts and roughly an order of magnitude more than the 8 km baseline with 18 LKFs (Tab. 3). This discrepancy is expected: although hybrid NN-FEM forms corrections on the auxiliary grid $\mathcal{T}_{\text{fine}}$, the accepted update is constrained to the working space $\mathcal{V}_{\text{coarse}}$. Some of the fine-scale features cannot be represented on the coarse mesh as the cells are too wide. Reproducing the 2 km LKF density is therefore not a meaningful target; the appropriate benchmark is the improvement relative to the 4 km resolution.

5.3.3. Metrics (M3) and (M4): Newton Iterations and Runtime.

Fig. 7 relates the time-to-solution T_{mom} for the sea-ice momentum equation to (a) the error E_{ℓ^2} (Fig. 7a) and (b) the LKF count N_{LKF} (Fig. 7b). Runtime scales primarily with the total number of Newton iterations N_{Newton} . The favorable region (low error, low time) is dominated by $N_M = 1$ and $N_M = 2$ configurations: for $N_M = 2$, networks with two layers of width 256 are particularly efficient. For $N_M = 1$, four layers of width 512 (or eight layers of width 256) achieve similar errors at comparable or slightly lower times, but with slightly fewer LKFs. While $N_M = 0$ leads to fast runtimes, it reduces the error only modestly. Hence, the best accuracy-efficiency trade-offs are $N_M = 1$ with a medium-large network and $N_M = 2$ with a compact network.

Fig. 8 decomposes the runtime T_{mom} (Fig. 8a) into the Newton-Krylov solver (Fig. 8b), memory copies for the network (Fig. 8c), and network evaluation (Fig. 8d), again as a function of N_M and (l, w) . Across all configurations, the Newton-Krylov solver dominates the wall time ($\sim 200\text{--}350$ s), whereas the DNN overhead (copies and inference) is $\mathcal{O}(10^{-1})$ s in total, i.e., $< 1\%$ of the runtime. Increasing the patch size N_M does not noticeably raise the cost of copies and inference. Although the network input and output sizes ($N_{\text{in}}, N_{\text{out}}$) grow with N_M and S (Tab. 2), their contribution to the runtime remains minor compared with the Newton-Krylov solver (cf. Fig. 8). The problem and data sizes do not saturate the available hardware. Total time scales with the total Newton iterations N_{Newton} (shown above the bars in Fig. 8), indicating an approximately constant per-iteration cost.

Network depth (2-8 layers) and width (128-512 units) have only a minor effect on runtime. For this reason, we only show results for $w = 256$ in Fig. 8. The inference cost T_{nn} grows slightly with network size but remains below 1 % of the numerical solver cost. Thus, further improvements of hybrid NN-FEM should primarily target a reduction of N_{Newton} . The copy and inference times each account for less than 1 % of the total runtime and have a minor impact on overall performance. We note that the timings reflect our hardware configuration: the numerical solver runs on the CPU, whereas the neural network is evaluated on the GPU. On systems with a different CPU/GPU balance or interconnect bandwidth the relative shares may change, but on typical hardware setups the qualitative conclusion, that the wall time is governed primarily by the total number of Newton iterations N_{Newton} , should remain valid.

The Newton and linear solvers are able to solve the nonlinear systems of equations, but are not fully h -robust for these equations: iteration counts increase with refinement and the per-iteration cost grows with the number of degrees of freedom. Consequently, the time to solution for the momentum equation at 2 km resolution exceeds that at 8 km by a factor ≈ 100 . In contrast, hybrid NN-FEM applied on the 8 km grid achieves both lower error and lower time-to-solution than the 8 km baseline (Fig. 7, Fig. 8). The cost of data generation in the experiments is essentially a single simulation of the benchmark at 2 km resolution. On our hardware, training a single network took less than a minute across the tested configurations, as training is not compute-bound for these small models.

5.3.4. Overall Performance Summary.

We summarize the discussed performance of the NN-FEM approach in Section 5.3.1-5.3.3. Across all runs, the *patch size* N_M is the dominant driver of prediction quality, while the *jump level* S has a secondary influence and the *architecture* (l, w) primarily shifts absolute LKF counts without changing the overall ranking (Tab. 3a-3c versus Tab. 3d-3f).

Compared to the coarse baseline simulation performed on the 8 km, which has $T_{\text{mom}} = 277.8$ s, $E_{\ell^2} = 0.528$, $N_{\text{LKF}} = 18$, and $N_{\text{Newton}} = 680$, the compact hybrid NN-FEM configuration at $S = 2$, $N_M = 1$ with $(l = 4, w = 256)$ achieves $T_{\text{mom}} = 252.45$ s (-9.1% compared to 8 km), $E_{\ell^2} = 0.042$, $N_{\text{LKF}} = 39$ (about $2.2\times$ the 8 km baseline), and $N_{\text{Newton}} = 551$ (-19%). The 4 km reference requires $T_{\text{mom}} = 2751.16$ s ($\approx 10.9\times$ the hybrid NN-FEM runtime), with $N_{\text{LKF}} \approx 51$. Across all tested hybrid NN-FEM settings, T_{mom} lies in

the narrow range 250–262 s, and the network overhead (copies and inference) remains $< 1\%$ of T_{mom} (Fig. 8). In summary, hybrid NN-FEM on the 8 km grid attains accuracy and LKF statistics comparable to the 4 km reference at roughly one-tenth of the Newton run-time of the high-resolution simulations, while keeping the additional neural network overhead negligible.

5.4. Ablation Studies on Neural Network Inputs

We test the *causal* role of network inputs by masking them while keeping architecture, weights, data, and the solver as well as finite element pipeline fixed. In particular, we assess the importance of the state and residual inputs by masking them in the batched input

$$\mathbf{X} = [\mathbf{v}_{\text{batched}} \mid \mathbf{r}_{\text{batched}} \mid \boldsymbol{\omega}].$$

Geometry $\boldsymbol{\omega}$ is kept unchanged, as it is constant across the whole batch (uniform Cartesian refinement). A masked input is *dispensable* if stability is unchanged (no divergence, no increase in N_{Newton} (M3)) and accuracy degrades at most marginally; otherwise it is *essential*. Removing $\mathbf{v}_{\text{batched}}$ tests *state-awareness* (local Jacobian scaling), removing $\mathbf{r}_{\text{batched}}$ tests *residual-awareness* (magnitude/direction), cf. Remark 4.3. Poor neural network predictions usually leads to residual growth and Newton divergence.

So far, we considered $\mathbf{X}_{\text{full}} = [\mathbf{v}_{\text{batched}} \mid \mathbf{r}_{\text{batched}} \mid \boldsymbol{\omega}]$. The goal is to compare the performance of hybrid NN-FEM when one of the inputs is masked:

$$\mathbf{X}_{(\mathbf{v}_{\text{batched}}=0)} := [\mathbf{0} \mid \mathbf{r}_{\text{batched}} \mid \boldsymbol{\omega}], \quad \mathbf{X}_{(\mathbf{r}_{\text{batched}}=0)} := [\mathbf{v}_{\text{batched}} \mid \mathbf{0} \mid \boldsymbol{\omega}].$$

For each $\alpha \in \{\mathbf{v}_{\text{batched}} = 0, \mathbf{r}_{\text{batched}} = 0\}$, we evaluate the network and assemble the correction as in Section 4.4,

$$\mathbf{D}_{(\alpha)} = \mathcal{N}(\mathbf{X}_{(\alpha)}), \quad \delta\mathbf{v}_{\text{fine},(\alpha)} = \mathbf{B}\mathbf{W} \sum_M S_M \mathbf{D}_{(\alpha);M,:}, \quad \mathbf{v}_{\text{fine},(\alpha)} = \mathbf{v}_{\text{fine}} + \delta\mathbf{v}_{\text{fine},(\alpha)}.$$

Inter-step Effect of the Hybrid NN-FEM Correction. The hybrid NN-FEM update is applied *after* Newton has converged at t^{n+1} and thus perturbs only the right-hand side of the *next* step. As discussed in Remark A.1, standard inexact Newton considerations suggest that this perturbation must be appropriately scaled relative to the unperturbed residual to retain local convergence. We therefore regard the hybrid NN-FEM correction as a controlled perturbation and *test* this expectation via input ablations.

Ablation ($\mathbf{v}_{\text{batched}} = 0$): Residual-only Input. We evaluate the residual-only variant by zeroing the state block in the batched network input. In all experiments, the correction constructed within hybrid NN-FEM increased the nonlinear residual and the subsequent Newton iteration diverged, yielding no usable solutions. On a patch N_M , an ideal stabilizing update solves (approximately) the local linearized equation $\mathcal{J}|_M(\mathbf{v})\delta\mathbf{v}|_M \approx -\mathbf{R}|_M(\mathbf{v})$ with $\mathcal{J}|_M(\mathbf{v}) = \partial_{\mathbf{v}}\mathcal{R}|_M(\mathbf{v})$, (cf. (14)) Using the splitting time approach to approximate the sea-ice dynamics the Jacobian of the momentum equation (11), $\mathcal{J}|_M(\mathbf{v})$, depends on the strain-rate invariants through $\eta(\mathbf{v}), \zeta(\mathbf{v})$ and is therefore state dependent and anisotropic. Masking $\mathbf{v}_{\text{batched}}$ forces the network to produce $\delta\mathbf{v}|_M$ without access to this local scaling/rotation. While this may still reduce a *same-step* fine-grid residual in expectation, it provides no control of the forcing in the next time step. Empirically, the correction $\delta\mathbf{v}_{\text{fine}}$, and, in turn, the perturbation of \mathbf{f}_{fine} becomes too large (or misaligned), such that condition (20) presented in the Appendix is not fulfilled anymore and the next Newton solve diverges. Thus, the state input is necessary to calibrate $\delta\mathbf{v}_{\text{fine}}^{n+1}$ to the local Jacobian and keep the perturbation induced by $\delta\mathbf{v}_{\text{fine}}$ within admissible bounds.

Ablation ($\mathbf{r}_{\text{batched}} = 0$): State-only Input. We evaluate the state-only variant by zeroing the residual block in the batched network input. Similar to the state ablation study, the hybrid NN-FEM correction leads to diverging Newton iterations and unusable solutions. If the residual block is masked, the network outputs $\delta\mathbf{v}_{\text{fine}}$ with no dependence on the local residual. Consequently, $\delta\mathbf{v}_{\text{fine}}^n$ does not scale with the *current* residual and, in particular, does not vanish when the residual is small. The perturbation of \mathbf{f}_{fine} induced by $\delta\mathbf{v}_{\text{fine}}^n$ is then uncontrolled in magnitude and direction relative to the residual, again causing Newton divergence at t^{n+1} due to the violation of condition (20) stated in the Appendix.

Because the hybrid NN-FEM correction acts *between* time steps as an explicit forcing, we conclude that stability requires *both* (i) state information $\mathbf{v}_{\text{batched}}$ to approximate the local action of $\mathcal{J}(\mathbf{v})^{-1}$ (scaling/rotation), and (ii) residual information $\mathbf{r}_{\text{batched}}$ to set the correct direction and scale. Masking either input destroys this coupling, yields a destructive perturbation, and destabilizes the Newton-Krylov solve in the next time step. This confirms our hypothesis in Remark 4.3. However, at this point, we do not prove a general guarantee beyond the empirical observations made here.

6. Conclusion

In this paper, we developed a hybrid NN-FEM approach to efficiently simulate sea-ice deformation, in particular linear kinematic features (LKF), on coarse horizontal grids. This is especially advantageous given that, in the viscous-plastic model, resolving LKFs typically requires grids with high spatial resolution. The hybrid NN-FEM approach for the viscous-plastic sea-ice model augments an under-resolved finite element solution with patch-local neural corrections, evaluated in a richer auxiliary space and subsequently assembled into a global correction. The construction preserves Dirichlet conditions.

With regard to the simulation of LKFs, our parameter study shows that patch size (the union of neighboring mesh elements of the fine grid), N_M , is the most important influencing factor. Larger patches provide a richer state context and better alignment with dominant deformation modes. We observe that an increasing number of refinement levels used in the training of the NN leads to a more accurate representation of LKFs, although this effect is less dominant than an increased patch size. A larger jump ($S = 2$) enables the correction to account for finer structures. The network depth and width mainly shift the absolute values of the LKFs and have a weaker influence on their representation quality compared to increasing S . In terms of accuracy-efficiency, $N_M = 2$, $S = 2$ with a compact MLP (two hidden layers, width 256) performs best. When training data are scarce, $N_M = 1$, $S = 2$ offers a stable trade-off with comparable runtime and slightly fewer LKFs. In our analysis, we observe that very large patches ($N_M = 3$) are data-sensitive. This is likely due to the fact that the feature dimension grows while the number of statistically independent patches per snapshot decreases, which can induce noisy corrections unless substantially more data (or stronger inductive bias) are available.

Across all settings, the nonlinear and linear solves dominate the runtime of solving the sea-ice momentum equation as typical for the sea-ice dynamics. The NN overhead (copies and inference) remains below 1 % on standard CPU/GPU nodes. The learned correction even accelerates the Newton method compared to the reference Newton solve on the coarse grid. In this setup, the solution of the momentum equation is up to 10 % faster with the NN-FEM approach than without the NN correction. Moreover, the hybrid NN-FEM elevates a 8 km baseline approximation to a level of accuracy qualitatively comparable to a 4 km discretization, while the 4 km run is nearly 11× more expensive than the hybrid NN-FEM.

The data requirements of very large patches suggest benefits from additional inductive bias (e.g., equivariance to rotations/reflections) or adaptive patching. A possible direction is *online*, semi-supervised training with physics-aware objectives that penalize fine-space momentum residuals after correction and incorporate stability cues from local sensitivity information. Such training has the potential to reduce labeled-data needs, improve generalization across different forcing terms and meshes, and further

decrease Newton iterations without increasing network capacity.

A. Technical Details of the Hybrid Neural Network-Finite Element Method

In Alg. 2 the correction at t^n modifies the state $\mathbf{v}_{\text{coarse}}$ obtained in Alg. 2, l. 2 at t^n . Thereby, the hybrid NN-FEM modifies the time integrator, as the previous state is used in the backward Euler at t^{n+1} . Hence, the hybrid NN-FEM correction in the current time step alters the right-hand side of the next step. Implementation-wise, we assemble all *load* terms on an auxiliary fine space using the corrected field and obtain the right-hand side in $\mathcal{V}_{\text{coarse}}$ by *restriction*. The notation below makes this restriction/prolongation precise. The subsequent remarks state the modified right hand side \mathbf{f}_{fine} assembly and quantify the perturbation through the correction, together with a simple smallness condition that guarantees admissibility for the inexact Newton solve at t^{n+1} . Beforehand, we need to introduce some additional notation.

To define the restricted right-hand side, we use the restriction and prolongation operators between the fine and coarse spaces. Let $f_{\text{fine}} \in \mathcal{V}_{\text{fine}}$. Its *restriction* to the coarse space $\mathcal{V}_{\text{coarse}}$ is defined by the Petrov-Galerkin duality

$$(\mathbf{R}f_{\text{fine}}, \mathbf{w}_{\text{coarse}}) := (f_{\text{fine}}, \mathbf{P}\mathbf{w}_{\text{coarse}}) \quad \forall \mathbf{w}_{\text{coarse}} \in \mathcal{V}_{\text{coarse}}.$$

In discrete form, if \mathbf{f}_{fine} denotes the assembled fine-grid right-hand side with entries $(\mathbf{f}_{\text{fine}})_i = (f_{\text{fine}}, \varphi_{\text{fine}_i})$, then the restricted coarse right-hand side is obtained by

$$\mathbf{f}_{\text{coarse}} = \mathbf{R}\mathbf{f}_{\text{fine}}, \quad \text{with} \quad \mathbf{R} = \mathbf{P}^\top.$$

Remark A.1 Impact of the correction on inexact Newton admissibility . Let $\mathcal{R}_{L,\text{base}}(\cdot)$ denote the residual built in $\mathcal{V}_{\text{coarse}}$ with the *uncorrected* history state $\mathbf{v}_{\text{coarse}}$, and let \mathcal{R} be the residual built with the *corrected* state. The modification is an additive functional

$$\mathcal{R}(\mathbf{v}_{\text{coarse}}, \mathbf{w}_{\text{coarse}}; \delta\mathbf{v}_{\text{fine}}) = \mathcal{R}_{\text{base}}(\mathbf{v}_{\text{coarse}}, \mathbf{w}_{\text{coarse}}) + \mathbf{g}_{\text{fine}}(\delta\mathbf{v}_{\text{fine}}, \mathbf{w}_{\text{coarse}}),$$

where

$$\mathbf{g}_{\text{fine}}(\delta\mathbf{v}_{\text{fine}}, \mathbf{w}_{\text{coarse}}) = \left(\frac{\rho}{k} \delta\mathbf{v}_{\text{fine}}, \mathbf{P}\mathbf{w}_{\text{coarse}} \right).$$

Let $\mathbf{v}_{\text{coarse}}^{(0)} \in \mathcal{V}_{\text{coarse}}$ be the initial Newton guess at t^{n+1} (typically the state from t^n). By the triangle inequality,

$$| \|\mathcal{R}(\mathbf{v}_{\text{coarse}}^{(0)}, \mathbf{w}_{\text{coarse}}; \delta\mathbf{v}_{\text{fine}})\| - \|\mathcal{R}_{\text{base}}(\mathbf{v}_{\text{coarse}}^{(0)}, \mathbf{w}_{\text{coarse}})\| | \leq \|\mathbf{g}_{\text{fine}}\|.$$

Thus, if

$$\|\mathbf{g}_{\text{fine}}\| \leq \beta \|\mathcal{R}_{\text{base}}(\mathbf{v}_{\text{coarse}}^{(0)}, \mathbf{w}_{\text{coarse}})\|, \quad \beta \in (0, 1), \quad (19)$$

then

$$(1 - \beta) \|\mathcal{R}_{\text{base}}(\mathbf{v}_{\text{coarse}}^{(0)}, \mathbf{w}_{\text{coarse}})\| \leq \|\mathcal{R}(\mathbf{v}_{\text{coarse}}^{(0)}, \mathbf{w}_{\text{coarse}}; \delta\mathbf{v}_{\text{fine}})\| \leq (1 + \beta) \|\mathcal{R}_{\text{base}}(\mathbf{v}_{\text{coarse}}^{(0)}, \mathbf{w}_{\text{coarse}})\|. \quad (20)$$

Let $\eta_0 \in [0, 1)$ denote the inexact Newton forcing parameter controlling the relative accuracy of the linear solve in the first Newton step. The inexact Newton linear solve at the first step is imposed on the *perturbed* residual:

$$\|\mathcal{R}(\mathbf{v}_{\text{coarse}}^{(0)}, \mathbf{w}_{\text{coarse}}; \delta\mathbf{v}_{\text{fine}}) + \mathcal{J}_{\text{coarse}}(\mathbf{v}_{\text{coarse}}^{(0)})[\delta\mathbf{v}_{\text{coarse}}^{(0)}, \mathbf{w}_{\text{coarse}}]\| \leq \eta_0 \|\mathcal{R}(\mathbf{v}_{\text{coarse}}^{(0)}, \mathbf{w}_{\text{coarse}}; \delta\mathbf{v}_{\text{fine}})\|, \quad \eta_0 < 1,$$

and the above bound (20) ensures that, provided the unperturbed guess lies in the local Newton convergence region, the perturbed one remains in the convergence region (with a radius reduced at most by the factor $1 + \beta$). Thus, one should enforce the bound (19).

B. Data Statistics

In this section, we summarize the main characteristics of the data sets used in our study. We report descriptive statistics for the training and test data as described in Sec. 5.2. This includes ranges and distributions of the input parameters and relevant output quantities (see Tab. 4 for grouped statistics of inputs (R_x, R_y, V_x, V_y) and outputs (u_1, u_2) by patch size N_M and jump level S).

C. Extended Results from the Numerical Experiments

In this section we report extended timing results for the hybrid NN-FEM solver. Fig. 9 provides a detailed breakdown for $S = 2$ across patch sizes $N_M \in \{0, 1, 2\}$ and all tested network widths and depths, showing total runtime, Newton-Krylov solver time, host-device copy time, and network inference time; the numbers above the bars indicate the total number of Newton iterations N_{Newton} . These data complement the timing results shown in Fig. 8 by including all considered network architectures and patch-size/jump-level configurations.

References

- [1] R. Becker et al. “The Finite Element Toolkit GASCOIGNE”. In: *Zenodo* (2021). <https://gascoigne.math.uni-magdeburg.de/>. doi: [10.5281/zenodo.5574969](https://doi.org/10.5281/zenodo.5574969).
- [2] E. Blockley et al. “The Future of Sea Ice Modeling: Where Do We Go from Here?” In: *Bulletin of the American Meteorological Society* 101.8 (2020), pp. 1304–1311.
- [3] S. Danilov et al. “Finite-Element Sea Ice Model (FESIM), version 2”. In: *Geosci. Model Dev.* 8 (2015), pp. 1747–1761. doi: [10.5194/gmd-8-1747-2015](https://doi.org/10.5194/gmd-8-1747-2015).
- [4] Ron S. Dembo, Stanley C. Eisenstat, and Trond Steihaug. “Inexact Newton methods”. In: *SIAM Journal on Numerical Analysis* 19.2 (1982), pp. 400–408. doi: [10.1137/0719025](https://doi.org/10.1137/0719025).
- [5] Charlotte Durand et al. “Data-driven surrogate modeling of high-resolution sea-ice thickness in the Arctic”. In: *The Cryosphere* 18 (2024), pp. 1791–1815. doi: [10.5194/tc-18-1791-2024](https://doi.org/10.5194/tc-18-1791-2024).
- [6] Stanley C. Eisenstat and Homer F. Walker. “Choosing the forcing terms in an inexact Newton method”. In: *SIAM Journal on Scientific Computing* 17.1 (1996), pp. 16–32. doi: [10.1137/0917003](https://doi.org/10.1137/0917003).
- [7] Tobias S. Finn et al. “Deep learning subgrid-scale parametrisations for short-term forecasting of sea-ice dynamics with a Maxwell elasto-brittle rheology”. In: *The Cryosphere* 17 (2023), pp. 2965–2991. doi: [10.5194/tc-17-2965-2023](https://doi.org/10.5194/tc-17-2965-2023).
- [8] G. Gao et al. “An unstructured-grid, finite-volume sea ice model: Development, validation, and application”. In: *Journal of Geophysical Research: Oceans* 116.C8 (2011).
- [9] W.D. Hibler. “A dynamic thermodynamic sea ice model”. In: *J. Phys. Oceanogr* 9 (1979), pp. 815–846. doi: [https://doi.org/10.1175/1520-0485\(1979\)009<0815:ADTSIM>2.0.CO;2](https://doi.org/10.1175/1520-0485(1979)009<0815:ADTSIM>2.0.CO;2).
- [10] E. Hunke et al. *CICE: the Los Alamos Sea Ice Model Documentation and Software User’s Manual Version 5.1* LA-CC-06-012. 2015.
- [11] J.K. Hutchings, P. Heil, and W.D. Hibler. “Modeling linear kinematic features in sea ice”. In: *Mon. Weather Rev.* 133 (2005), pp. 3481–3497.
- [12] N. Hutter and M. Losch. “Feature-based comparison of sea ice deformation in lead-permitting sea ice simulations”. In: *The Cryosphere* 14.1 (2020), pp. 93–113. doi: [doi:10.5194/tc-14-93-2020](https://doi.org/10.5194/tc-14-93-2020).

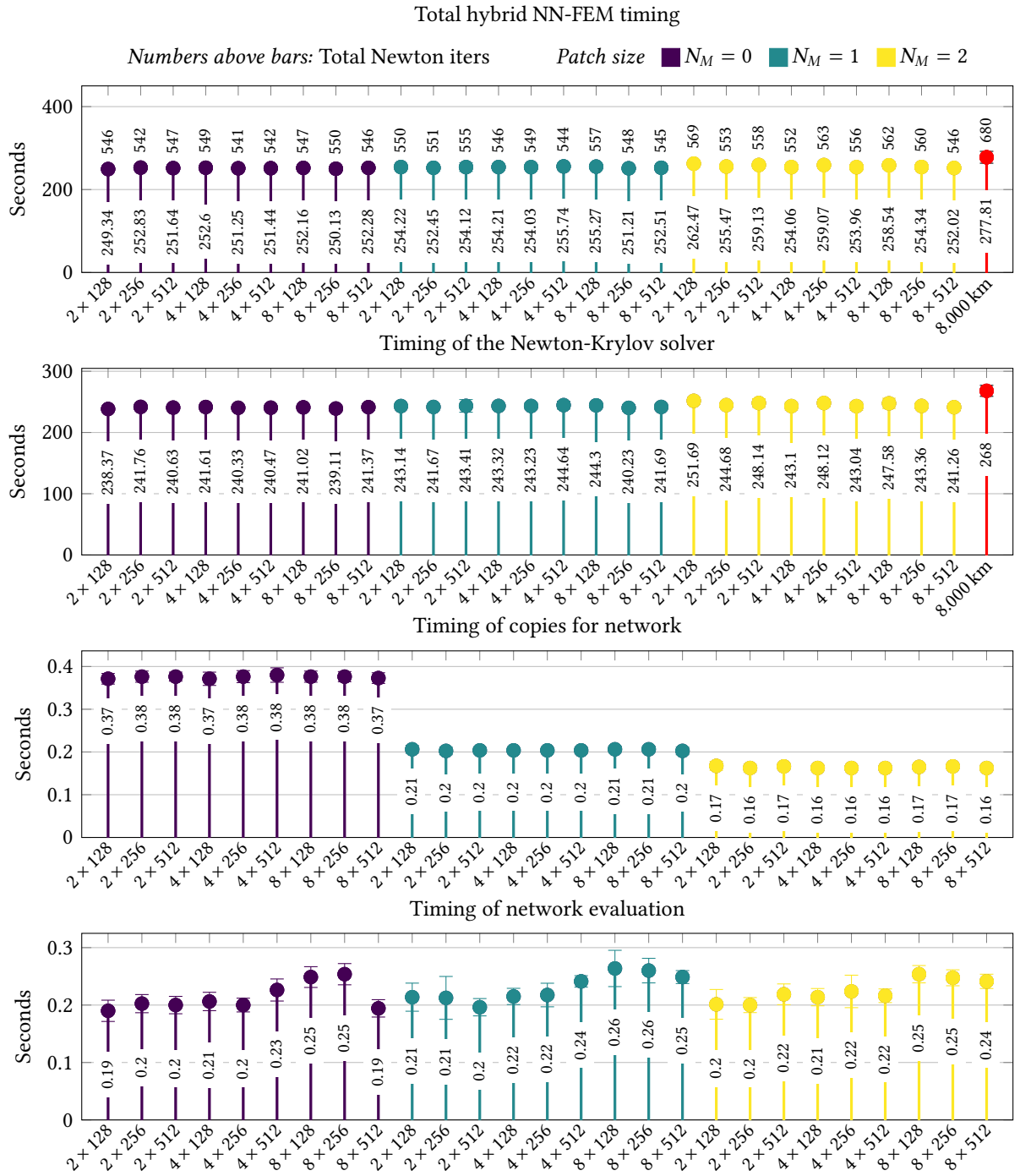


Figure 9: Timing of hybrid NN-FEM for $S = 2$ across patch sizes $N_M \in \{0, 1, 2\}$ (colors) and network widths/depths: total runtime, Newton-Krylov solver time, host-device copy time, and network inference time; numbers above bars denote total Newton iterations N_{Newton} .

[13] N. Hutter et al. “Sea Ice Rheology Experiment (SIREx): 2. Evaluating Linear Kinematic Features in High-Resolution Sea Ice Simulations”. In: *Journal of Geophysical Research: Oceans* 127.4 (2022), e2021JC017666 2021JC017666, e2021JC017666. doi: <https://doi.org/10.1029/2021JC017666>. eprint: <https://agupubs.onlinelibrary.wiley.com/doi/pdf/10.1029/2021JC017666>. URL: <https://agupubs.onlinelibrary.wiley.com/doi/abs/10.1029/2021JC017666>.

[14] Nils Hutter. *lkf_tools: a code to detect and track Linear Kinematic Features (LKFs) in sea-ice deformation data (Version v1.0)*. code. Zenodo. 2019. doi: [10.5281/zenodo.2560078](https://doi.org/10.5281/zenodo.2560078). URL: [http://doi.org/10.5281/zenodo.2560078](https://doi.org/10.5281/zenodo.2560078).

[15] N. Koldunov et al. “Fast EVP Solutions in a High-Resolution Sea Ice Model”. In: *Journal of Advances in Modeling Earth Systems* 11.5 (2019), pp. 1269–1284.

[16] M. Kreyscher et al. “Results of the Sea Ice Model Intercomparison Project: Evaluation of sea ice rheology schemes for use in climate simulations”. In: 105 (2000), pp. 11299–11320.

[17] R. Kwok et al. “Variability of sea ice simulations assessed with RGPS kinematics”. In: 113.C11 (2008).

[18] J.F. Lemieux et al. “A comparison of the Jacobian-free Newton-Krylov method and the EVP model for solving the sea ice momentum equation with a viscous-plastic formulation: a serial algorithm study”. In: *Journal of Computational Physics* 231 (2012), pp. 5926–5944.

[19] M. Losch et al. “On the formulation of sea-ice models. Part 1: Effects of different solver implementations and parameterizations”. In: *Ocean Modelling* 33.1 (2010), pp. 129–144.

[20] Ilya Loshchilov and Frank Hutter. “Decoupled Weight Decay Regularization”. In: *International Conference on Learning Representations* (2019).

[21] Nils Margenberg, Christian Lessig, and Thomas Richter. “Structure Preservation for the Deep Neural Network Multigrid Solver”. In: *Electronic Transactions on Numerical Analysis* 56 (2022), pp. 86–101. doi: [10.1553/etna\vol56s86](https://doi.org/10.1553/etna\vol56s86).

[22] Nils Margenberg et al. “A neural network multigrid solver for the Navier–Stokes equations”. In: *Journal of Computational Physics* 460 (2022), p. 110983. doi: [10.1016/j.jcp.2022.110983](https://doi.org/10.1016/j.jcp.2022.110983).

[23] Nils Margenberg et al. “DNN-MG: A Hybrid Neural Network/Finite Element Method with Applications to 3D Simulations of the Navier-Stokes Equations”. In: *Computer Methods in Applied Mechanics and Engineering* 420.C (2024), p. 116692. doi: [10.1016/j.cma.2023.116692](https://doi.org/10.1016/j.cma.2023.116692).

[24] Gary A. Maykut. “Energy exchange over young sea ice in the central Arctic”. In: *Journal of Geophysical Research: Oceans* 83.C7 (1978), pp. 3646–3658. doi: <https://doi.org/10.1029/JC083iC07p03646>.

[25] C. Mehlmann and P. Korn. “Sea-ice dynamics on triangular grids”. In: *J. Comput. Phys.* 428 (2021), p. 110086. doi: <https://doi.org/10.1016/j.jcp.2020.110086>.

[26] C. Mehlmann et al. “Simulating Linear Kinematic Features in Viscous-Plastic Sea Ice Models on Quadrilateral and Triangular Grids With Different Variable Staggering”. In: *Journal of Advances in Modeling Earth Systems* 13.11 (2021), e2021MS002523. doi: <https://doi.org/10.1029/2021MS002523>.

[27] Carolin Mehlmann and Thomas Richter. “A modified global Newton solver for viscous-plastic sea ice models”. In: *Ocean Modelling* 116 (2017), pp. 96–107. doi: [10.1016/j.ocemod.2017.06.001](https://doi.org/10.1016/j.ocemod.2017.06.001).

[28] A. Paszke et al. “PyTorch: An Imperative Style, High-Performance Deep Learning Library”. In: *Advances in Neural Information Processing Systems* 32. Ed. by H. Wallach et al. Curran Associates, Inc., 2019, pp. 8024–8035. URL: <http://papers.neurips.cc/paper/9015-pytorch-an-imperative-style-high-performance-deep-learning-library.pdf>.

- [29] M. Petersen et al. “An Evaluation of the Ocean and Sea Ice Climate of E3SM Using MPAS and Inter-annual CORE-II Forcing”. In: *Journal of Advances in Modeling Earth Systems* 11.5 (2019), pp. 1438–1458.
- [30] P. Rampal et al. “neXtSIM: a new Lagrangian sea ice model”. In: *The Cryosphere* 10 (2016), pp. 1055–1073.
- [31] Y. Shih et al. “Robust and efficient primal-dual Newton-Krylov solvers for viscous-plastic sea-ice models”. In: *Journal of Computational Physics* 474 (2023), p. 111802. ISSN: 0021-9991. DOI: <https://doi.org/10.1016/j.jcp.2022.111802>.
- [32] Leslie N. Smith. “Cyclical Learning Rates for Training Neural Networks”. In: *2017 IEEE Winter Conference on Applications of Computer Vision (WACV)*. 2017, pp. 464–472. DOI: [10.1109/WACV.2017.58](https://doi.org/10.1109/WACV.2017.58).
- [33] Maximilian Witte et al. “Dynamic deep learning based super-resolution for the shallow water equations”. In: *Machine Learning: Science and Technology* 6.1 (2025), p. 015060. DOI: [10.1088/2632-2153/ada19f](https://doi.org/10.1088/2632-2153/ada19f).

Table 4: Grouped statistics (mean, std, min, max) for inputs (R_x, R_y, V_x, V_y) and outputs (u_1, u_2) by patch size N_M and jump level S . Geometry rows are omitted.

N_M	S	Kind	Group	mean	std	min	max
0	1	In	R_x	1.835×10^{-11}	2.159×10^{-9}	-4.515×10^{-8}	4.115×10^{-8}
		In	R_y	-4.057×10^{-11}	2.074×10^{-9}	-4.654×10^{-8}	4.120×10^{-8}
	1	In	V_x	1.396×10^{-6}	6.358×10^{-5}	-1.614×10^{-4}	1.790×10^{-4}
		In	V_y	8.122×10^{-7}	6.354×10^{-5}	-1.590×10^{-4}	1.789×10^{-4}
	1	Out	u_1	9.456×10^{-9}	1.834×10^{-6}	-4.082×10^{-5}	5.715×10^{-5}
		Out	u_2	-1.158×10^{-7}	2.956×10^{-6}	-9.292×10^{-5}	5.715×10^{-5}
0	2	In	R_x	-1.449×10^{-11}	9.306×10^{-10}	-2.589×10^{-8}	2.278×10^{-8}
		In	R_y	6.604×10^{-12}	9.730×10^{-10}	-2.251×10^{-8}	2.233×10^{-8}
		In	V_x	1.185×10^{-6}	6.363×10^{-5}	-1.637×10^{-4}	1.796×10^{-4}
		In	V_y	1.005×10^{-6}	6.354×10^{-5}	-1.590×10^{-4}	1.796×10^{-4}
		Out	u_1	2.524×10^{-8}	2.898×10^{-6}	-7.451×10^{-5}	1.013×10^{-4}
		Out	u_2	-2.257×10^{-7}	4.438×10^{-6}	-1.047×10^{-4}	1.016×10^{-4}
1	1	In	R_x	-1.328×10^{-11}	2.218×10^{-9}	-4.654×10^{-8}	4.115×10^{-8}
		In	R_y	3.784×10^{-12}	2.152×10^{-9}	-4.530×10^{-8}	4.120×10^{-8}
		In	V_x	1.345×10^{-6}	6.343×10^{-5}	-1.590×10^{-4}	1.790×10^{-4}
		In	V_y	8.703×10^{-7}	6.355×10^{-5}	-1.614×10^{-4}	1.776×10^{-4}
		Out	u_1	4.491×10^{-8}	1.829×10^{-6}	-4.213×10^{-5}	5.715×10^{-5}
		Out	u_2	-1.598×10^{-7}	3.138×10^{-6}	-9.292×10^{-5}	5.715×10^{-5}
1	2	In	R_x	2.182×10^{-12}	9.274×10^{-10}	-2.566×10^{-8}	2.233×10^{-8}
		In	R_y	-4.701×10^{-12}	9.449×10^{-10}	-2.589×10^{-8}	2.278×10^{-8}
		In	V_x	1.294×10^{-6}	6.348×10^{-5}	-1.590×10^{-4}	1.796×10^{-4}
		In	V_y	8.985×10^{-7}	6.361×10^{-5}	-1.637×10^{-4}	1.788×10^{-4}
		Out	u_1	5.850×10^{-8}	2.942×10^{-6}	-7.469×10^{-5}	1.013×10^{-4}
		Out	u_2	-2.652×10^{-7}	4.561×10^{-6}	-1.047×10^{-4}	1.016×10^{-4}
2	1	In	R_x	1.727×10^{-12}	2.275×10^{-9}	-4.654×10^{-8}	4.061×10^{-8}
		In	R_y	-9.101×10^{-13}	2.192×10^{-9}	-4.530×10^{-8}	4.120×10^{-8}
		In	V_x	1.813×10^{-6}	6.306×10^{-5}	-1.488×10^{-4}	1.741×10^{-4}
		In	V_y	4.034×10^{-7}	6.380×10^{-5}	-1.614×10^{-4}	1.790×10^{-4}
		Out	u_1	4.593×10^{-8}	1.893×10^{-6}	-3.297×10^{-5}	5.715×10^{-5}
		Out	u_2	-1.638×10^{-7}	3.203×10^{-6}	-9.292×10^{-5}	5.715×10^{-5}
2	2	In	R_x	-1.981×10^{-13}	9.122×10^{-10}	-2.566×10^{-8}	2.278×10^{-8}
		In	R_y	8.691×10^{-13}	9.515×10^{-10}	-2.589×10^{-8}	2.114×10^{-8}
		In	V_x	1.824×10^{-6}	6.314×10^{-5}	-1.488×10^{-4}	1.765×10^{-4}
		In	V_y	3.681×10^{-7}	6.389×10^{-5}	-1.637×10^{-4}	1.796×10^{-4}
		Out	u_1	5.532×10^{-8}	3.003×10^{-6}	-6.884×10^{-5}	1.013×10^{-4}
		Out	u_2	-2.630×10^{-7}	4.598×10^{-6}	-1.047×10^{-4}	1.016×10^{-4}